Appendix A

Quantum Cascade Photonic Crystal Surface-Emitting Injection Lasers

A.1 Introduction

In this appendix, I review the results of a collaborative project between our group at Caltech and the quantum cascade (QC) laser group at Bell Laboratories, aimed at the development of photonic crystal microcavity lasers within quantum cascade heterostructures. The results I described are the focus of refs. [34, 35, 36]. Unlike the main part of this thesis, the focus here was not on the development of high-Q, small-V_{eff} resonators for cavity QED, but to instead utilize other important properties of planar PC cavities, such as their scalability and potential for surface emission, to create novel QC lasers, termed QC-PCSELs (quantum cascade, photonic crystal surface-emitting lasers). In addition, another main distinction in comparison to the PC lasers studied in chapter 3 is that these QC PC lasers are electrically injected devices. As electrical injection is a desirable characteristic for many devices, some of the techniques utilized in this work are of potential significance for applications involving high Q, small V_{eff} PC lasers.

Research in semiconductor heterostructures has led to the development of a number of optoelectronic devices in which the flow of electrons is controlled with great precision [194]. The quantum cascade laser [195, 196], one product of such progress in electronic bandstructure engineering, operates based upon intraband optical transitions (within conduction band states, or subbands) where electrons flow through a semiconductor superlattice ”staircase”, emitting a photon at each step. Such devices are hence unipolar (single carrier), and thus operate in a fundamentally different manner than standard semiconductor lasers, which rely upon electron-hole recombination for light generation. QC lasers have established themselves as the leading tunable coherent semiconductor source

in the mid- and far-infrared (IR) ranges of the electromagnetic spectrum [197, 198, 199].

However, due to the transverse magnetic (TM) polarization of intersubband transitions, QC lasers are intrinsically only in-plane emitters. The electric field vector is perpendicular to the semiconductor layers, and surface emission, desirable for several applications, cannot be easily achieved. The PC microcavity that we employ acts both as a source of optical feedback and as the means for diffracting light vertically from the chip to provide surface emission. In addition to enabling surface emission, our devices are greatly scaled down from standard QC devices, enabling miniaturization and on-chip integration of QC lasers, with potential applications such as multi-wavelength two-dimensional laser arrays for spectroscopy envisioned. In addition, QC PC lasers are an interesting system for research on photonic bandgap structures, as their unipolar nature, operation through electrical injection, and long emission wavelengths (and hence larger device feature sizes) are unique and advantageous aspects in comparison to previously studied interband PC lasers. In particular, the demonstration of an electrically-injected PC microcavity laser is an important step in the development of PC technology for practical applications.[1] In our QC PC lasers, an etched pattern penetrates through the laser active region, deep into the bottom waveguide cladding. This etch produces the same 2D PC pattern in the lower refractive index bottom cladding as in the waveguide core, allowing for efficient vertical confinement of the guided mode [201]. This design reduces the diffraction of radiation into the substrate, while providing a high-index contrast semiconductor-air 2D grating for strong in-plane feedback. As a result, our devices use only 10 periods of the photonic lattice (less than eight wavelengths in diameter), hence, their classification as microcavity lasers.

A.2 Basic design and fabrication

The details of the device design and measurement are given elsewhere (ref. [34] and references therein). For our purposes here, the key background information is an overview of the principles of the device operation and an understanding of the PC design strategy. fig. A.1(a) shows a schematic view of a QC-PCSEL device. Electronic current transport through a cascade of active regions and injectors within the QC heterostructure results in photon emission at $\lambda \sim 8\ \mu$m. Optical feedback is provided by a PC microcavity consisting of an array of air holes that has been etched through the active region and bottom cladding of the QC heterostructure. The lattice of air holes provides distributed Bragg reflection (DBR) in two dimensions parallel to the chip.

[1] At the time of publication of this work, the QC PC lasers described here were the first electrically injected PC microcavity lasers. Since that time, electrically injected PC lasers at near-IR wavelengths have also been demonstrated[200].

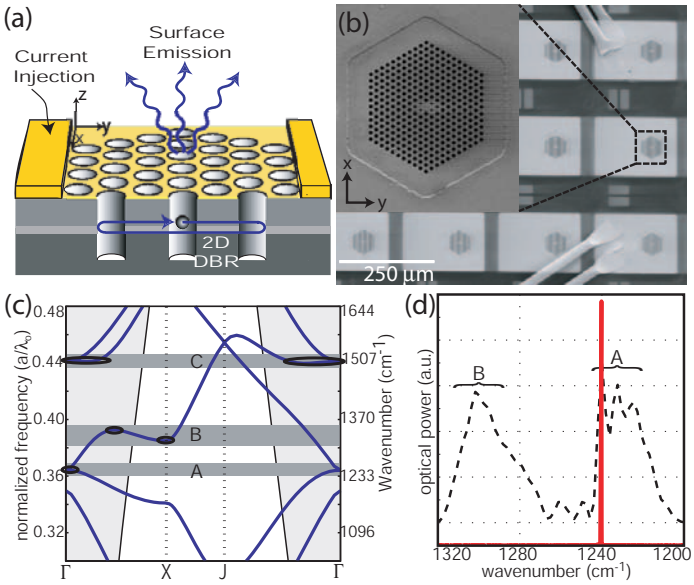

Figure A.1: (a) Schematic of a QC-PCSEL device. (b) Scanning electron microscope (SEM) image of an array of QC-PCSELs (inset shows a zoomed in top-view of a device). (c) Calculated two-dimensional in-plane TM bandstructure. The flat-band regions (A, B, and C) are indicated by dark gray bands. (d) Sub-threshold (dashed) and lasing (solid) emission spectra from a QC-PCSEL with lattice geometry tailored for emission centered at the A flat-band region.

The PC lattice consists of a hexagonal array of air holes, chosen primarily due to its connected nature (unlike a lattice of rods, for example), necessary for efficient electrical injection. The intersubband transitions in quantum wells are naturally TM-polarized (electric field normal to the epitaxial layers). Using the plane-wave expansion method [202], we thus calculate the in-plane bandstructure for TM modes, shown in fig. A.1(c) for a device with hole radius (r) to lattice constant (a) ratio $r/a = 0.30$, and with an effective index $n_{\text{eff}} = 3.35$ taken to account for vertical waveguiding. Highlighted in this bandstructure are three frequency regions of interest, labeled A, B, and C, which overlap flat-band regions. These flat-band regions are formed through mixing of forward and backward propagating plane waves at high-symmetry points of the PC reciprocal lattice. In these flat-band regions, low-loss resonant modes can be localized in finite lattice structures (such as our cavities) due to the reduction in group velocity over an extended region of wavevector space. Regions A, B, and C are specifically highlighted because they surround the flat-band regions in the frequency range close to the second-order Bragg condition. Close to the second-order Bragg condition, light can radiate into the air for surface emission, as coupling occurs to plane waves with near-zero in-plane momentum. These are the components which lie above the air-light cone (light gray region of fig. A.1(c)) and can radiate vertically. Choosing $a \sim 3$ μm for a hexagonal lattice with r/a=0.30 aligns these flat-band regions with the QC material gain spectrum ($\lambda \sim 8$ μm).

Vertical optical confinement is determined by the semiconductor and metal layers comprising the QC laser structure. A key element of our design is the use of a surface-plasmon waveguide

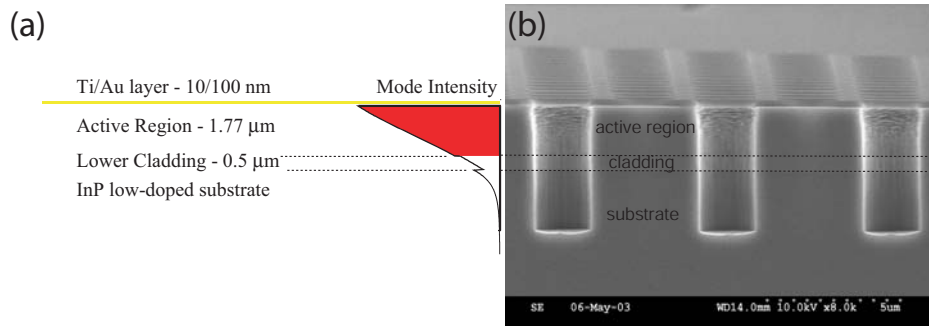

Figure A.2: (a) QC epitaxy and surface plasmon waveguide mode. (b) Cross-sectional SEM of an etched QC PC laser.

for vertical confinement [203]. This waveguide exhibits an electric field intensity maximum at the top semiconductor-metal interface (fig. A.2(a)). Particularly relevant to this work is the thinner epitaxial material (2.4 μm compared with 5.2 μm for a standard waveguide) and the absence of AlInAs cladding layers. Both of these characteristics dramatically ease the etching process, which must penetrate into the bottom InP cladding to suppress radiation into the substrate [201].

The PC patterns are created by electron beam lithography, mask transfer to a dielectric oxide layer, and transfer into the heterostructure material by inductively-coupled plasma reactive ion etching. The deep etch through the vertical waveguide core region into the bottom cladding layer (see appendix C) produces a high index contrast semiconductor-air grating (fig. A.2(b)), reducing substrate radiation losses and ensuring that only a small number of PC periods (less than 8 optical wavelengths in diameter) are required to provide strong optical feedback, in contrast to traditional second order grating based devices which typically employ a shallow etch (weak grating) and require several hundred periods of the lattice.

After etching of the PC pattern, an insulating silicon nitride layer is deposited surrounding the PC cavities, and top and back metal contact layers are evaporated, with the etched sidewalls sufficiently vertical to prevent electrical shorting. In addition, a thin metal layer, used to create the bound surface plasmon mode in the vertical direction of the waveguide, is evaporated on the surface of the cavities. An array of fully-processed QC-PCSEL devices is shown in fig. A.1(b).

A.3 Electroluminescence and lasing measurements

As described in ref. [34], low-temperature electroluminescence measurements of microfabricated devices reveal three sets of emission peaks, corresponding to regions *A*, *B*, and *C* in fig. A.1(c).

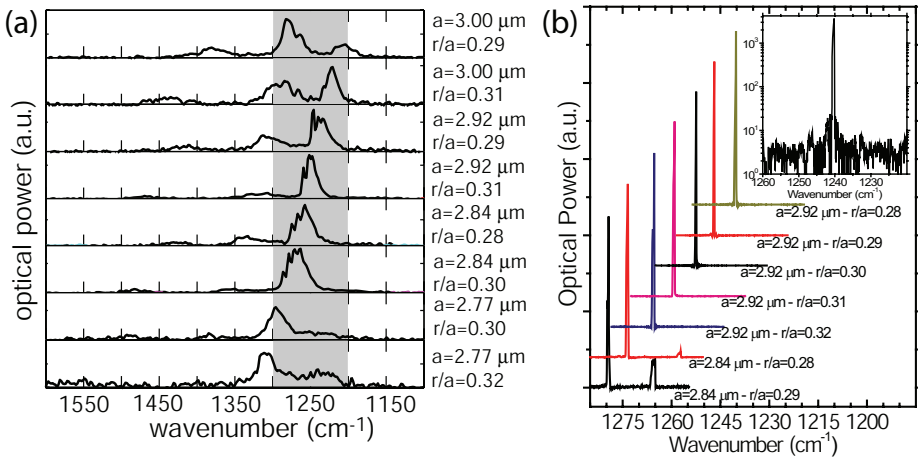

Figure A.3: (a) Emission spectra from devices with different a and r/a. The gray shaded area corresponds to the FWHM of the QC gain spectrum.(b) Tuning of the laser emission wavelength as a function of a and r/a for several different devices located on the same semiconductor chip. The lasers operate predominantly in single mode (see inset) with a side-mode suppression of at least 20 dB.

Laser emission was achieved (operating in pulsed mode with 50 ns pulse width at 5 kHz repetition rate), and is seen to tune with the hole radius and lattice spacing of the PC cavity in accordance with simulation predictions (fig. A.3). Figure A.1(d) shows the subthreshold and lasing emission spectra for a device with lattice geometry chosen to align the gain peak to the *A* flat-band region. Lasing always originated from the highest frequency (wavenumber) resonance within the *A*-peak. The majority of the devices exhibit single mode laser emission in pulsed mode. By selecting devices with different values for a or r, multi-wavelength emission from the same semiconductor chip is achieved (fig. A.3).

As described in ref. [36], a careful analysis of the experimental data (spectral information, far-field emission measurements and polarized intensity measurements) and numerical simulations shows a close correspondence between theory and simulation, and provides a unique identification of the lasing mode. The first step in the process of identification of the laser mode is to determine its symmetry. Here, we consider the behavior of the laser mode under reflection about the cavity's $\hat{x}$ and $\hat{y}$ axes (see fig. A.1(b) for the definition of these axes with respect to the cavity). The polarized spatial distribution of the laser's vertically emitted field intensity is studied by placing a polarizer in front of a micro-bolometer camera fitted with a lens (fig. A.4(a-b)). The nodal lines (lines of near-zero intensity in the images) along the $\hat{x}$ and $\hat{y}$ axes of fig. A.4(b) for the $\hat{y}$-polarized intensity pattern are consistent exclusively with an electromagnetic field mode which is odd (parity -1) under

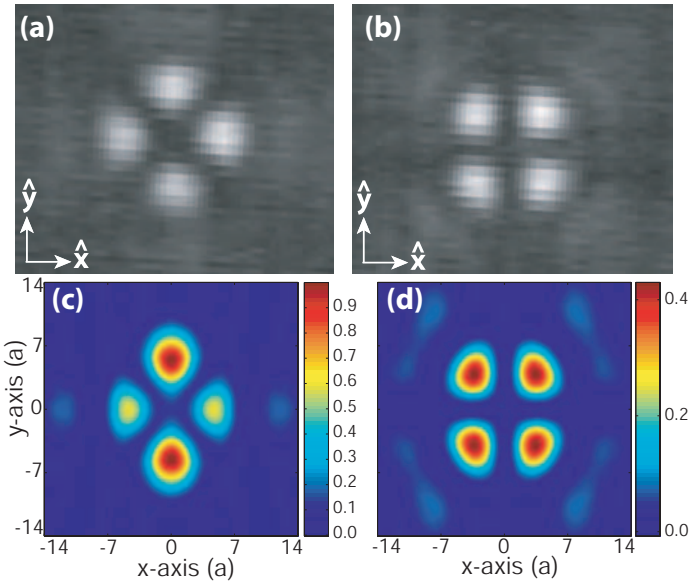

Figure A.4: (a) Polarized emission pattern (taken in a plane close to the near field of the PC cavity surface) of a typical lasing device for an electric field polarization along the (a) $\hat{x}$-axis and (b) $\hat{y}$-axis of the cavity. FDTD-generated (c) $\hat{x}$-polarized and (d) $\hat{y}$-polarized vertical emission pattern at a few wavelengths above the PC cavity.

a mirror symmetry about the $\hat{y}$-axis and which is even (parity +1) under a mirror symmetry about the $\hat{x}$-axis. Such a mode is said to have B_1 symmetry, using the nomenclature of chapter 1. A similar conclusion is reached by studying the $\hat{x}$-polarized intensity pattern of fig. A.4(a), which has anti-nodes along both the $\hat{x}$- and $\hat{y}$-axis. Thus, the two polarized intensity patterns of fig. A.4(a-b) indicate that the laser emission is single mode and of B_1 symmetry.

To better understand the vertical emission characteristics of the PC microcavity modes, full 3D-FDTD simulations were performed. The hole depth was taken to be 5 microns and a 200 nm thick idealized 'perfectly conducting' metal top contact was used to guide the TM surface wave (at a wavelength of 8 μm this is a reasonable approximation for a gold metal contact [204, 93]). To reduce the size and time of the simulation, the cavity was limited to 6 periods of the hexagonal lattice as opposed to the 10 periods used in the experiment. Mirror boundary conditions were used to project the modes of the hexagonally symmetric cavity onto a basis compatible with the symmetry of a rectangle whose principal axes lie along the $\hat{x}$- and $\hat{y}$-axis of the PC microcavity.

The highest frequency resonant mode of the A-peak was found to be of B_1 symmetry (we refer to this mode simply as the B_1 mode from here on). This is consistent with the experimentally measured emission spectrum (fig. A.1(d)) and with the laser near field symmetry (fig. A.4(a-b)). Figure A.5(a-b) shows the electric field component normal to the semiconductor-metal surface (E_z) and its in-plane spatial Fourier transform ($\widetilde{E}_z$) for the B_1 mode. It is interesting to note that this mode has only a small overlap with the central region of the PC cavity, a characteristic which

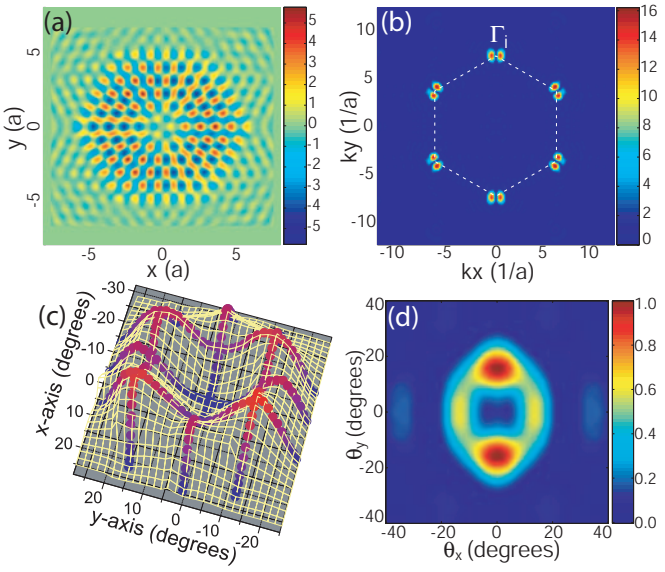

Figure A.5: FDTD-generated plot of (a) E_z and (b) $\widetilde{E_z}$ for the B_1 mode in the plane of the PC cavity just beneath the metal contact in the semiconductor active region. (c) Far-field emission pattern of the PC microcavity laser. The experimental data is shown as blue/red dots, and an interpolation of the line scans (shown as a light yellow grid) is used to generate an approximate 2D intensity image. (d) FDTD simulation of the far-field intensity pattern for the high-frequency mode within the *A*-peak set of resonances.

may partially explain its preferential selection as the lasing mode, due to the expected in-plane spreading resistance in the etched PC region and consequent higher current injection and gain in the periphery of the PC. Calculations of the vertically emitted radiation field, taken in a plane several wavelengths above the cavity surface, were performed by eliminating the non-propagating FDTD near field components and introducing, to simulate the experimental conditions, a 30° collection angle cut-off for the imaging optics. The resulting $\hat{x}$- and $\hat{y}$- polarized intensity patterns of the B_1 mode are shown in fig. A.4(c-d), and closely match the polarized micro-bolometer camera images (fig. A.4(a-b)).

As a final consistency check, far-field emission measurements and calculations were performed. Figure A.5(c) shows a typical far-field intensity pattern of the B_1 lasing mode, measured by scanning a 300×300 μm nitrogen-cooled HgCdTe detector in a plane parallel to the semiconductor chip surface at a distance of approximately 10 cm without any intermediate optics. The theoretical far-field emission pattern was calculated by transforming the FDTD generated radiation field into the far-field [205] and is shown in fig. A.5(d). The increased intensity of the two lobes on the $\hat{y}$-axis in fig. A.4(c) of the $\hat{x}$-polarized intensity and in fig. A.5(d) of the far-field pattern is likely a result of inadvertent symmetry breaking of the hexagonal symmetry of the PC cavity in the FDTD simulation.[2] In this case, the computed near field under the metal contact is still very symmetric, as shown in fig. A.5(a). The symmetry breaking in the measured far field (experimentally we observe

[2]This may result from discretization error in employing the mirror boundary conditions and/or the rectangular boundary of the simulation volume.

the opposite effect, more intensity in the $\hat{y}$-polarization), is possibly a result of the rectangular metal contact geometry and/or non-uniform current injection.

The FDTD-calculated radiative quality factor (Q) of the B_1 mode was found to be roughly a factor of two higher than the Q value of the neighboring A-peak resonant modes, helping explain why it is the first mode to lase. The calculated in-plane, top, and substrate radiation rates, as given by effective cavity quality-factors, were $Q_{\|}$=600, Q_t=10,000, and Q_s=7,000, respectively. An estimate for the Q value associated with internal loss in the metal and semiconductor at 8 microns ($\alpha_i = 40\ cm^{-1}$) is Q_a=800. Thus, the total vertical extraction efficiency of the PC microcavity laser is estimated to be $\eta_t = Q_t^{-1}/(Q_{\|}^{-1} + Q_t^{-1} + Q_s^{-1} + Q_a^{-1}) = 3\%$. The vertical extraction of light in this case is due to the radiation of small in-plane Fourier components near the Γ-point of the hexagonal PC reciprocal lattice (fig. A.5(b)), as in second-order Bragg diffraction. The coupling of radiation from the bottom semiconductor-metal interface to the top metal-air interface (from which the radiation finally escapes) is mediated through the air holes [204], as well as through the metal itself (although this last effect has not been included in our simulations).

These PC microcavity lasers combine the electronic bandgap engineering exploited in QC lasers and the optical dispersion engineering of photonic crystals. The result is a photonic crystal injection laser that may open new horizons in device design and application in the mid- to far-IR ranges of the electromagnetic spectrum. In particular, multi-wavelength surface emission makes these devices interesting from the perspective of spectroscopy applications, as many trace gases and complex molecules can be probed in this wavelength region [206, 207]. The open cavity architecture of these holey devices makes them interesting from the perspective of integration with fluids; microfluidic technology [208, 209] can, in principle, be integrated with these devices to allow for precise delivery of these fluids to the cavity regions. The introduction of the fluid should affect the L-I characteristic (light out versus injected current) of the device, for example, through a modification of the laser threshold current. Electrical readout (a kind of 'detectorless' spectroscopy) within these systems is a promising possibility with QC-PCSEL-based devices.

Significant improvements in device performance must be made in order for these applications to become accessible. In particular, the operating temperature must be increased, and the threshold current needs to be reduced. Current efforts, led by Raviv Perahia at Caltech, are focused on reducing current spreading in the devices as a means to help achieve these goals.

Appendix B

Finite-Difference Time-Domain Simulations

The photonic crystal cavities studied in this thesis are numerically investigated through the finite-difference time-domain (FDTD) method, reviewed in detail by Taflove [6]. The FDTD algorithm discretizes Maxwell's equation, replacing derivatives with finite differences that are second order accurate. The implementation that is commonly used is based on the Yee algorithm [210], which is essentially a direct solution to Maxwell's curl equations, solving for both the electric and magnetic fields in time and space. The Yee algorithm follows a grid (fig. B.1(a)) in which every electric field component (E) is surrounded by four circulating magnetic field components (H), and vice versa. This arrangement means that Faraday's and Ampere's laws (which are integral forms of Maxwell's equations) are automatically satisfied, as are Gauss's divergence laws. In terms of boundary conditions, this arrangement naturally assures the continuity of tangential field components across material boundaries that follow the cartesian grid.

FDTD is very appropriate for modeling structures such as our PC cavities, where the refractive index varies significantly on the sub-wavelength scale; other techniques that approximate Maxwell's equations with a wave equation usually require a slowly varying refractive index. In addition, because it does not require matrix inversion techniques, FDTD can be used to do full three-dimensional modeling of microphotonic structures. Accurate estimates of important properties such as the frequency, quality factor, and modal volume can be obtained.

The code that we use was originally written by Brian D'Urso, an undergraduate in Professor Axel Scherer's group at Caltech, and has since been modified by a number of graduate students. Full three-dimensional simulations of PC cavities are typically performed in the following fashion. To reduce the simulation time, only one-eighth of the cavity volume is simulated (the upper octant, for

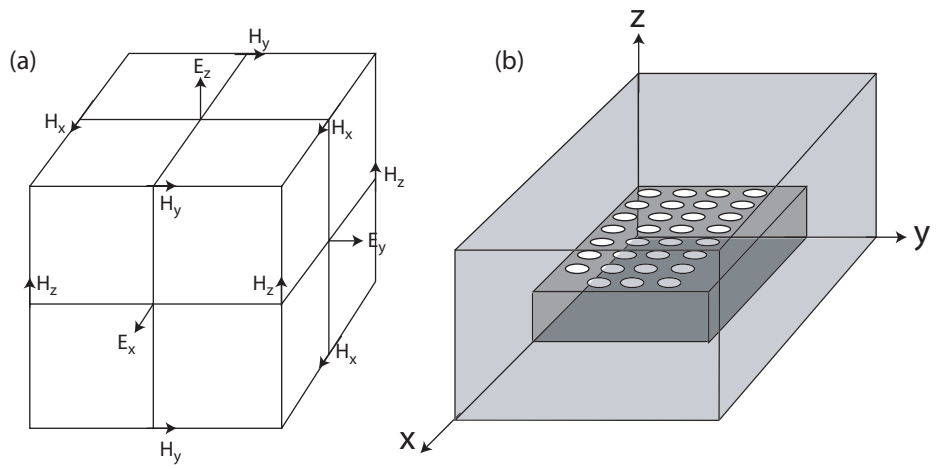

Figure B.1: Setup for FDTD simulations. (a) Yee space lattice, as formulated in ref. [210]. Figure adapted from ref. [6] (b) Typical simulation volume for 3D photonic crystal cavities. Mirror boundary conditions are applied along the planes x=0, y=0, and z=0; Mur's absorbing boundary conditions are applied along the other three faces of the simulation volume.

example), with mirror conditions chosen for three of the cavity boundaries. Absorbing conditions are chosen for the other three boundaries, and an air region, typically on the order of two-thirds of a free-space wavelength, is placed above the cavity to allow the field to adequately decay before it reaches the boundary. In the in-plane dimensions, the field has already decayed within the photonic crystal region so that only a small air region (or no air region at all) is needed in those dimensions. Figure B.1(b) shows a schematic of this. To adequately represent the field within the structure, we choose a discretization of 20 points per lattice constant (which typically translates to about 80 points per free space wavelength for the devices we study). With this resolution, the total number of grid points is typically on the order of 2×10^6 (200x200x50, for example).

To calculate the cavity mode field patterns in chapter 2, a two-step process is used. We first calculate the time evolution of an initial field placed within the cavity, and record this time evolution at some small number of judiciously chosen spatial points ($\sim$5-10). The initial field is a delta function in time and has a Gaussian spatial profile, and is chosen to have the polarization of interest (TE or TM). Modes of a specific symmetry can be chosen through proper choice of the mirror boundary conditions; alternately, if a full structure is simulated, the initial field is spatially located off-center to allow for excitation of modes of both even and odd spatial symmetry. The field as a function of time is fourier transformed to give its spectral content. Cavity modes appear as peaks within this spectrum.

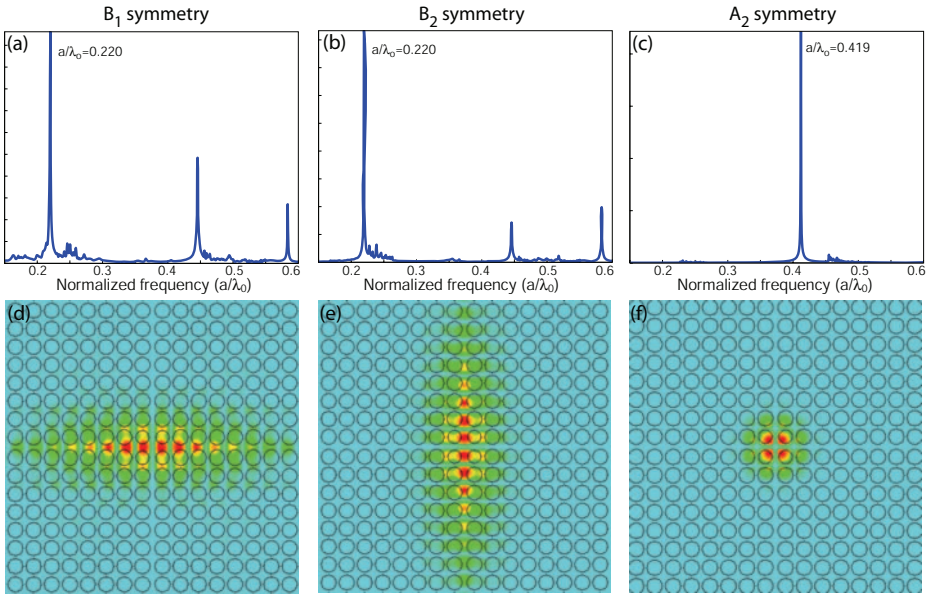

Figure B.2: FDTD spectra and mode field patterns for TM-polarized donor type defect modes in a square lattice photonic crystal. (a)-(c) Spectra for modes of (a) B_1, (b) B_2, and (c) A_2 symmetry. (d)-(f) $|\mathbf{E}|$ for the specified modes in (a)-(c)

Figure B.2(a)-(c) shows examples of such spectra, taken from ref. [37]. The system studied here is a simple square lattice donor-type defect centered about point e in the lattice (see chapters 1 and 2 for the labeling of high symmetry points in the square lattice), where we are focused on TM-polarized modes due to their applicability for QC lasers. From the group theory analysis of chapter 1 (extended to cover TM modes), we know that the two X-point donor type defect modes off the first conduction band are predicted to have B_1 and B_2 symmetry, and the donor type mode off the M-point of a higher frequency band is predicted to have A_2 symmetry. This knowledge allows us to specify the mirror boundary conditions; a separate simulation is run for each symmetry type (three simulations in all here).

The second step of the process is to determine the spatial field profiles for the cavity modes. To solve for the field profile for a given mode, we take the modal frequency determined through the spectral calculation described above, and use it as the center frequency for a bandpass filter. The initial field (chosen to have the appropriate polarization) is then convolved in time with the bandpass filter [211], whose width is slowly decreased as the initial field evolves and begins to stabilize. The cavity Q is calculated by determining the stored energy in the cavity (U) and the radiated power to the boundaries (P_d), with $Q = \omega U/P_d$. Example modal field patterns generated by this technique are shown in fig. B.2(d)-(f).

In the design of high-Q cavities presented in chapter 2, we made frequent use of the spatial Fourier transform of the cavity mode as a diagnostic tool for understanding radiation losses within a given design. In these calculations, we Fourier transform the complex field pattern $\mathbf{E}(\mathbf{r})$. By doing so, we capture all of the spatial Fourier components, regardless of the time at which the snapshot of the field is taken. The real, physical electric field can be written in terms of this complex field pattern as $\mathbf{E}(\mathbf{r},t) = (\mathbf{E}(\mathbf{r})e^{-i\omega_0 t} + \mathbf{E}^*(\mathbf{r})e^{i\omega_0 t})/2$. To generate the complex field pattern, we take snapshots of the real field at times t and $t + T/4$, where $T/4$ is a quarter period ($T = 2\pi/\omega_0$), so that $\mathbf{E}(\mathbf{r}) = \mathbf{E}(\mathbf{r},t) + i\mathbf{E}(\mathbf{r},t + T/4)$. Typically, the times are chosen so that they coincide with the magnetic field maximum (at time t, for example) and the electric field maximum (at time $t + T/4$).

Appendix C

Fabrication Notes

In this appendix, I have compiled some notes that, for the most part, focus on the etching of materials using an inductively coupled plasma reactive ion etch (ICP-RIE) tool. The initial part gives a general overview of some of the considerations taken into account when processing these materials when the focus is on the creation of microphotonic structures. I then consider fabrication within specific material systems that are relevant to this thesis, including Si, GaAs/AlGaAs, and the quantum cascade heterostructures considered in appendix A. As fabrication of photonic crystal cavities within the InP-based multi-quantum-well material was considered in detail in chapter 3, no specific further consideration of those devices is given here.

C.1 Process flow and general considerations

The process flow for fabricating a device such as a photonic crystal microcavity (fig. C.1) typically consists of 1) deposition of a hard mask layer (occasionally not required), 2) spin coating of the sample in electron beam resist and subsequent electron beam lithography, 3) plasma etching (also known as dry etching) of the mask layer, and 4) plasma etching of the primary material layer (typically a semiconductor layer in the applications we consider). For some devices, such as the passive PC resonators and optically pumped lasers described in this thesis, these steps are followed by a wet etch step to undercut the devices. For more complicated structures, such as electrically-contacted devices, a number of additional fabrication steps are required.

The creation of low loss optical devices requires an optimization of the steps listed above. For the plasma etching steps, there are a number of factors to take under consideration. One of the most important is the mask layer used during the etching; the strength and quality of the mask layer determines what types of etches can be used. Due to the small feature sizes needed for most of

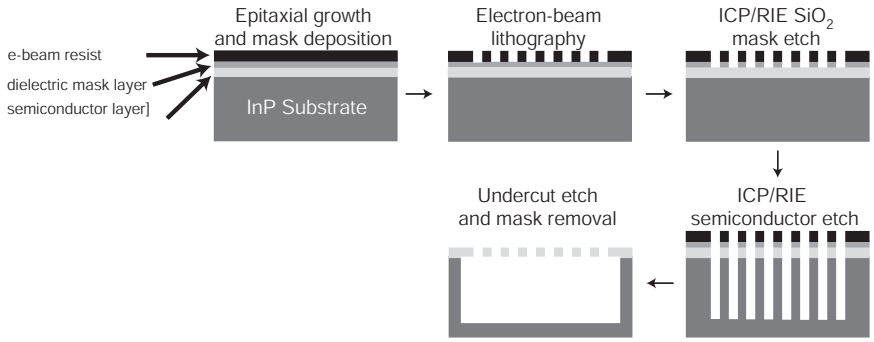

Figure C.1: Process flow for fabrication of microphotonic devices such as photonic crystals.

our structures, the starting point will always be an electron beam mask. A relatively soft mask (such as an electron beam resist mask) that is easily damaged through the dry etching procedures necessitates the use of a low impact dry etch, while harder masks such as dielectric layers provide greater etch selectivity and the ability to use a wider variety of etches, but come at the expense of having to develop a method to fabricate the dielectric mask. For semiconductor etches that are deeper than a few hundred nanometers, a hard mask is typically a necessity. For most of the devices we consider in this thesis (with the exception of the QC lasers), the required etch depth is just a couple hundred nanometers (corresponding to a half-wavelength of light in the material). In such cases, direct etching into the semiconductor using the electron beam resist is a possibility, although the benefits (and drawbacks) of this simpler approach must be weighed against the merits of using a dielectric mask. To use a dielectric mask, one has to develop a suitable etch recipe for transferring the pattern from the electron beam resist to the dielectric layer, and this can be, in some cases, as difficult as etching the semiconductor layer directly.

Once a masking material is chosen, the plasma etching processes can be calibrated. Plasma etching is used because of the anisotropic etch profiles that it can create; PC cavities, for example, require vertical sidewalls to sustain high Qs. Wet etching, on the other hand, can produce very smooth etched surfaces, but the etch profiles are often slanted and control of feature sizes can be difficult (due to undercutting of the mask layer). The system we use for plasma etching is an Oxford Instruments Plasma Technology (OIPT) ICP-RIE, which has the advantage of allowing for independent control of the plasma density (through variation of the ICP power) and the kinetic energy of the resulting ions (through application of RF power to the wafer table/electrode upon which the sample sits). This allows for the development of processes that employ a precise combination of chemical etching and physical etching (ion milling) to create anisotropic, smooth sidewalls. In addition,

we have control over gas chemistry (Ar, N_2, H_2, O_2, Cl_2, SF_6, and C_4F_8 are our available gases), chamber pressure, and sample temperature (either through control of the temperature of the lower electrode or the application of He to the backside of the sample). Typically, we begin development of an etch process by starting with an etch recipe provided by OIPT, or by searching the technical journals (particularly the *Journal of Vacuum Science and Technology B*) to see what work has been done by other groups. This essentially serves to give us a starting point, but the final etch is often quite different from this initial recipe. One reason for this is that the low loss, micro-optical structures of interest to us are often quite different than the applications for which many previous etch recipes have been developed, so that the requirements on the etch can also be significantly different. In addition, structures such as PCs contain very small confined spaces whose etch behavior is markedly altered relative to that of more open structures (both the delivery of source gases and the removal of etched by-products can be modified within these confined regions). Finally, most etch recipes in the literature are calibrated using photoresist, a dielectric layer, or a metal layer as an etch mask. While we will often use a dielectric etch mask immediately before etching of a semiconductor layer, the initial mask, where the cavity geometry is first defined, and from which the dielectric mask is created, is usually an electron beam layer.

Before considering the specific processes employed to create the structures studied in this thesis, let us review some of the process parameters involved in the plasma etching. The gas chemistry used is determined by the material system being etched; chlorine-based chemistries, for example, are known to be effective in etching III-V heterostructures, while fluorine-based chemistries are often used for silicon, silicon dioxide, and silicon nitride. Reference [212], for example, lists many of the common etch chemistries used to etch semiconductor materials. Once a chemistry is selected, gas flows must be chosen. Here, the important things to consider are the ratio of the gas flows (for example, the ratio of Ar to the ratio of Cl_2 when etching GaAs) and the total gas flow. The total gas flow needs to be chosen in such a way that a sufficient amount of gas reaches the sample (so that the etch is not reactant-limited), but should not be so high that the gas does not have a sufficient amount of time to react with the material. Typical total gas flows are on the order of 20-30 sccm (standard cubic centimeters per minute) for the processes we have used. The ratio of the gas flows will, among other things, affect the etched sidewall angle and smoothness; examples of this will be shown below.

The chamber pressure is another important process parameter. Typically, the chamber is held at a baseline pressure of $\sim 10^{-7}$ torr when no process is being run; typical process pressures are ~ 10

mTorr. The effect of the chamber pressure on the etch behavior can be somewhat difficult to gauge. In principle, if the etch is one in which chemical etching is the dominant mechanism, an increased chamber pressure will increase the concentration of the reactive elements and can speed up the etch (though the etch rate may eventually saturate). If the etch is primarily a physical milling process, an increased pressure will also initially increase the etch rate, but may eventually cause it to slow, as the increased pressure may cause collisions between ions that will reduce the kinetic energy with which they bombard the surface.

The ICP power level sets the density of ionized atoms. In addition, it can have an effect on the sample temperature; dense plasmas generated by high ICP powers can cause heating of the sample, which can dramatically influence the etch rate, sidewall profile, and sidewall roughness. This effect has been exploited in our etching of QC heterostructures, as described below in section C.4. The RF power level sets a DC Bias, which is basically a potential difference between the plasma coils and the lower electrode upon which the sample sits. This DC Bias drives the ions into the sample; a large DC Bias will impart significant kinetic energy into the ions, making physical etching a dominant process. A large ion milling component will significantly affect the etch mask as well, so that high DC Bias etches typically require use of a hard dielectric etch mask. In addition, a high DC Bias can heat the sample.

C.2 Si-based devices

We have been able to create high aspect ratio Si PC structures through direct transfer using an electron beam resist; this has basically been made possible as a result of the relative ease with which Si can be etched and the relatively thin ($\sim$ 350 nm) waveguide layer we employ in our devices. The starting point for our process was an OIPT recipe that called for a relatively low RF power (50 W), a high ICP power (1200 W), and a C_4F_8/SF_6 etch chemistry. This was a very appealing etch in that it did not require the special operating conditions that other Si etches do (such as cryo-cooling or gas chopping).

The first step in the etch calibration was to determine the gas flows to be used. This was done by fixing a total gas flow and varying the ratio of C_4F_8 to SF_6. The behavior of the etch as a function of this ratio was very controllable; higher SF_6 flows would increase the verticality of the etch (though flows that are too high would undercut the mask), while C_4F_8 could be used to smoothen the sidewalls and counteract the chemical etching by SF_6. After a suitable flow ratio was chosen,

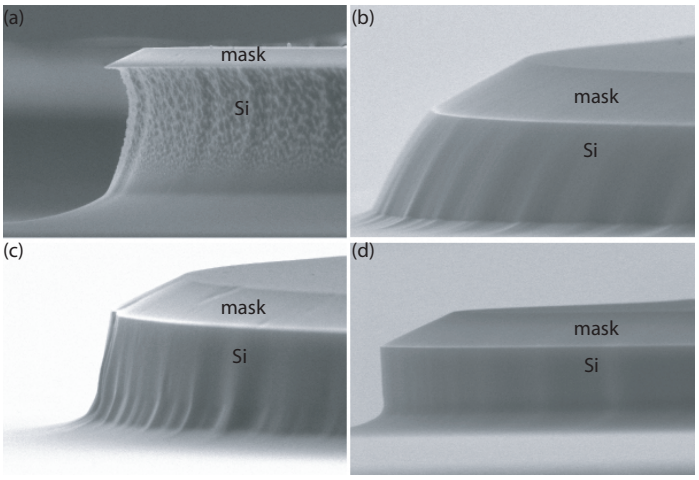

Figure C.2: SEM images of the Si ICP-RIE etch with varying gas flow and RF power. (a) RF=50 W, C_4F_8=11 sccm, SF_6=12 sccm (b) RF=50W, C_4F_8=22 sccm, SF_6=12 sccm (c) RF=50W, C_4F_8=11 sccm, SF_6=12 sccm (d) RF=20W, C_4F_8=11 sccm, SF_6=12 sccm.

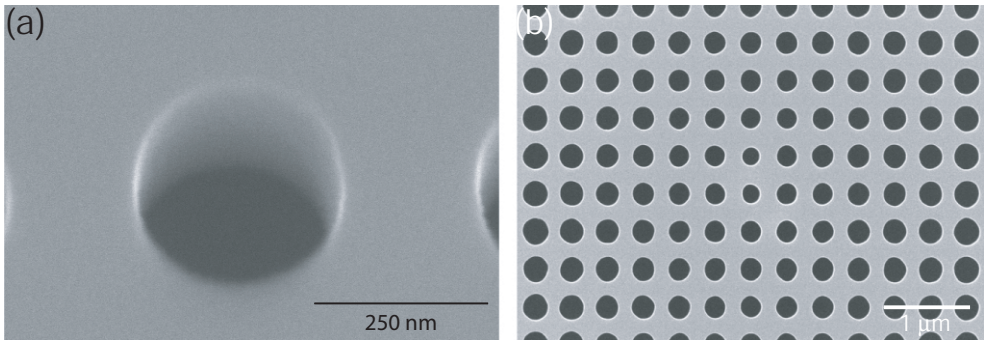

Figure C.3: (a) Angled and (b) top view SEM images of the Si etch used in fabrication of high-*Q* PC cavities.

the RF power was varied to limit mask erosion as much as possible. Figure C.2 shows SEM images of an etched sidewall as function of different process parameters. The initial etch calibration was done using a photoresist mask consisting of a relatively large circle. After a reasonable etch had been achieved with this mask, PC patterns in an electron beam resist were used in the final etch optimization. The primary modification here in comparison to the process used in fig. C.2(d), for example, is a further reduction in RF power and a bit of an increase in the C_4F_8 gas flow. Figure C.3(a) shows an angled SEM image of an etched PC pattern, showing the sidewalls to be both smooth and vertical. Figure C.3(b) is a top view SEM image of an etched structure, indicating that the holes are smooth and circular, which is a good indication that the etch that has been employed does not significantly damage the electron beam mask, thereby allowing faithful transfer of the PC pattern into the Si layer.

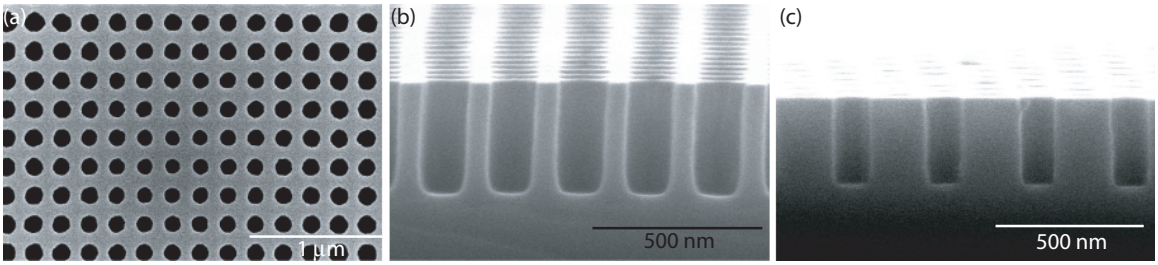

Figure C.4: Top view and cross sectional SEM images of AlGaAs PC cavities fabricated using an SiO_2 etch mask.

C.3 AlGaAs-based devices

As briefly mentioned in the preface, the GaAs/AlGaAs system dry etches with an ease that, qualitatively, is somewhere between Si (easy) and InP (hard). At the time we began our work on etching AlGaAs structures, we had already developed an etch recipe for InP using an SiO_2 mask (chapter 3), and our hope was to simply use this mask. We would then use some form of an Ar/Cl_2 chemistry to plasma etch the AlGaAs layer, and the PC membrane would be undercut with a dilute HF acid wet etch. In general, fabrication processes can be difficult to reproduce, as the condition of the etch chamber is continuously changing over time, particularly for chambers (such as ours) in which multiple materials are etched. As a result, even after a process has nominally been completely developed, there is often some kind of re-calibration period needed prior to fabrication of a new set of devices, particularly if it has been a few weeks since the last round of fabrication. When I started doing SiO_2 etches for the purpose of AlGaAs fabrication, it had been about 8 months since our InP-based PC microcavity laser work, and our ICP-RIE had mostly been used for Si etching during that time. For reasons that were never completely explainable, we were unable to replicate our previous success with the SiO_2 etch; the etch now seemed to burn the resist somewhat, and produced misshapen holes, even after many attempts at modifying the etch to make it less damaging to the resist. We were able to develop a subsequent AlGaAs etch that could produce smooth, vertical sidewalls for a range of hole sizes, but the problems we had with the lack of circularity in the holes seemed to be significant enough to warrant investigation of other masks. Figure C.4 shows the results of our AlGaAs processing with an SiO_2 etch mask. The AlGaAs etch employed was a simple derivative of the InP etch described in chapter 3, but now done at room temperature, with modifications to the Ar/Cl_2 gas flows (the Ar/Cl_2 ratio was now typically 10/5 sccm) and slight adjustments to the RF and ICP powers.

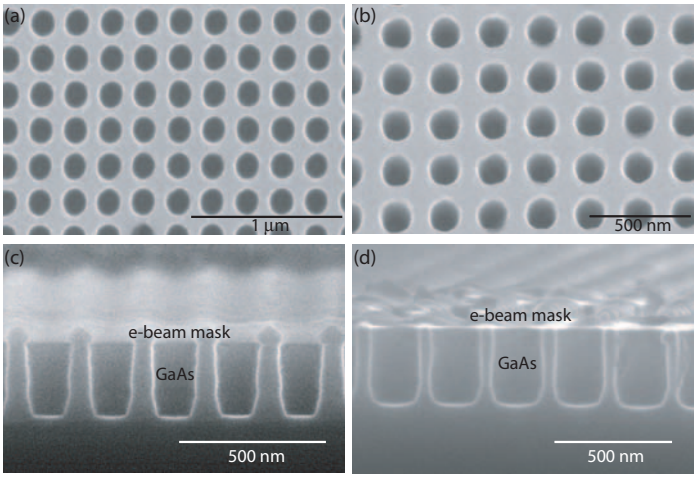

Figure C.5: SEM images of AlGaAs photonic crystals using direct pattern transfer from an electron beam mask. (a) top view, (b) angled view, and (c)-(d) cross sectional view, showing the different sidewall angles for different hole sizes.

Another possibility was to transfer the PC pattern directly from the electron beam resist to the AlGaAs layer. We spent a few weeks working this out, and developed a reasonably good AlGaAs etch that was able to do this while maintaining good hole shapes and without overly damaging the resist. This etch was again a derivative of the InP etch, performed at room temperature, with significantly lower RF powers (now $\sim$70 W) and an Ar/Cl_2 gas ratio of $\sim$10/5 sccm. The electron beam resist seemed to be less adversely affected by the Ar/Cl_2 chemistry (in terms of the hole shape) than the C_4F_8/O_2 chemistry used to etch the SiO_2, even though the RF power and DC Bias levels used were fairly similar. However, maintaining sidewall verticality over the range of hole sizes used in our graded lattice designs was difficult, and it was clear that the etch did undercut the electron beam mask, so that producing a desired hole size would take some amount of calibration (this seemed particularly difficult in that the hole size varies widely in our graded lattice design). As angled sidewalls can cause a significant increase in loss in planar photonic crystals [114], we decided that a dielectric etch mask would probably be a necessity. The advantage in using a dielectric mask is that the range of RF powers that can be used is significantly larger (with the electron beam mask, we had to limit the RF power to avoid etching the mask away too quickly or beginning to burn the mask). Nevertheless, the direct transfer approach, summarized by the SEM images in fig. C.5, remains a potentially viable option, particularly if further optimization can be done to help improve the sidewall verticality.

In order to etch a dielectric mask without burning the electron beam resist, we wanted to adopt an etch that would be similar to what we used for Si, where we were able to transfer the PC patterns into the Si device layer while only using an electron beam mask. This did not seem far-fetched,

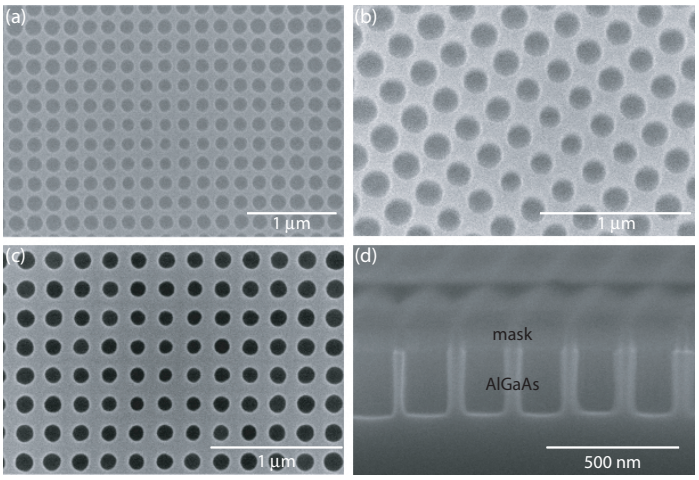

Figure C.6: SEM images of photonic crystal patterns in a SiN_x mask and subsequent transfer into AlGaAs. (a)-(b) Top view and angled image of the SiN_x mask. (c)-(d) Top view and cross sectional image of the AlGaAs layer using the SiN_x as an etch mask.

as both Si and SiO_2 can be dry etched using a fluorinated chemistry. However, when we tried to etch the SiO_2 with this low RF power etch, it was not very successful; the etch proceeded very slowly and the sidewalls were not vertical. Another option for the mask was SiN_x, which we could also deposit with our PECVD. The nitride mask was a great choice, primarily because it could be effectively etched using essentially the same conditions as what we used for Si. The etch rate was certainly much slower than what it was for Si, but on the positive side, the resist was not burned or misshapen during the etch, and we had a sufficiently thick resist layer to be able to etch through the nitride mask ($\sim$ 200 nm thick). Results for the nitride etch are shown in fig. C.6(a)-(b); typical process conditions were quite similar to the Si etch described above. Once this etch was developed, we used an AlGaAs etch (fig. C.6(c)-(d)) that was essentially identical to that used when we tried an SiO_2 mask, as the SiN_x had nearly the same etch selectivity.

We used the SiN_x and AlGaAs etches developed for PC cavities as a basis for etching the microdisk structures investigated in the second part of this thesis. The main difference in the etches were the gas chemistries and RF powers used; we typically decreased the chemical nature of the etches (increased C_4F_8 for the SiN_x, decreased Cl_2 for the AlGaAs), and slightly reduced the applied RF power. With the microdisk cavities, the primary objective is to make the disk sidewall smooth; this has led to us adopting etches where sidewall verticality has been sacrificed in favor of smoothness.

The SiN_x etch can be a bit unpredictable in practice. In particular, if the C_4F_8 flow is too low, the etched sidewalls can be very rough. Figure C.7 shows the results of some poor etches; the sidewall roughness in the mask is clearly transferred into the AlGaAs layer. As the state of our etching

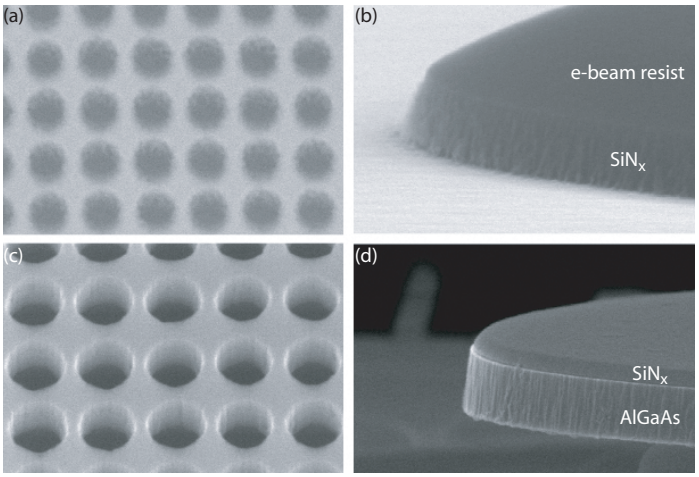

Figure C.7: SEM images of photonic crystal and microdisk patterns when the SiN_x etch does not turn out properly, most likely because of too low a flow of C_4F_8. (a)-(b) SiN_x PC and microdisk mask and (c)-(d) AlGaAs layer using the SiN_x as an etch mask.

chamber is essentially constantly varying in time, we typically have to re-calibrate the SiN_x etch before each new processing batch. This usually involves a couple of practice etches that are used to determine the precise C_4F_8 and SF_6 flows and RF power that will etch the material appropriately given the current state of the etch chamber. In addition, chamber cleaning runs are periodically run, in principle, to reset the condition of the chamber.

C.4 ICP-RIE etching of quantum cascade heterostructures

The quantum cascade lasers discussed in appendix A required a dry etch optimization to be able to create relatively deep ($\sim$ 4-5 μm), etched features ($\sim$2 μm diameter holes) with vertical sidewalls in an InP-based heterostructure. The starting point was a 500 nm thick SiO_2 mask (etched at Bell Laboratories) that had smooth and relatively vertical sidewalls ($> 85^\circ$). Our efforts on developing this etch are reported in ref. [35].

Dry etching of In-containing III-V semiconductor materials is typically accomplished using one of two gas chemistries [115]. The first, using a CH_4/H_2 mixture, is performed at room temperature but is relatively slow ($<$ 60 nm/min) and suffers from heavy polymer deposition during the process. Cl_2-based plasmas have also been used, but the low volatility of $InCl_x$ products at room temperature requires some form of heating to be employed. One method for producing smoothly etched, vertical sidewalls in an InP-based semiconductor system is direct heating of the wafer table ($> 150\,^\circ$C). Such a process was employed to etch the near-IR PC lasers of chapter 3, for example.

The Cl_2-based plasma etch that we discuss in this appendix does not make use of direct wafer table heating, but rather uses the high density plasma produced by the ICP system to provide local

surface heating of the sample and an increased efficiency in the sputter desorption of the $InCl_x$ products [115]. Such an etch has been used by Fujiwara et al., to etch 8 μm diameter, 3.6 μm deep holes in a photonic bandgap structure [116].

The ICP-RIE etch was studied as a function of ICP power (300-500 W) and RF power (100-350 W), with the chamber pressure (P_{ch} = 3 mTorr) and Ar:Cl_2 gas chemistry (12 sccm:8 sccm) kept fixed, and no He backside cooling. The final ICP and RF powers chosen were 350 and 250 W, respectively, and produced vertical sidewalls with an acceptable amount of sidewall roughness (fig. C.8). Lower RF powers produced extremely pitted (and slightly angled) sidewalls throughout both the core and cladding layers (which we attribute to the decreased volatility of the $InCl_x$ etch products, resulting from the lower sample temperature and/or lower desorption rate caused by the reduced RF power), while higher RF powers created smooth sidewalls in the lower cladding and InP layers but increased roughness in the core layer (attributed to pitting that occurs in Al-containing layers that are etched at too hot a temperature). Similar effects on the sidewall roughness were observed as the ICP power was varied. These results suggest that the sample temperature (generated by the plasma) is a leading factor affecting sidewall roughness. The percentage of Cl_2 in the gas mixture, which can also play a role, has been varied between 30% and 50%, with a value of 35% (7 sccm) finally chosen as the best compromise between decreased sidewall roughness (seen for lower Cl_2 percentages) and improved sidewall angle (seen for higher Cl_2 percentages). For our typical etch times (t$\sim$4.75 min), etch depths of 5 μm are achieved.

Using the plasma as a mean of increasing the sample temperature indicates that the etch rate (and therefore etch depth) will be a nonlinear function of time, as some amount of time is required for the temperature to reach a value hot enough for the $InCl_x$ compounds to be sufficiently volatile. This has been observed experimentally, as etch times under 3 min have produced devices with angled holes and non-volatile $InCl_x$ etch products. Note that the change in sample temperature as a function of time for a number of different process parameters has been investigated in detail by Thomas III et al. [213], and confirms that some minimum etch time (dependent upon the RF and ICP powers) is required for the sample to reach the requisite temperature ($> 150\,^{\circ}$C).

Our etch creates a nearly 90° sidewall angle but suffers from roughness in the core layer. We believe that this is the result of the elevated sample temperature created by the high density plasma, which probably causes pitting of Al-containing layers. In the optimal case, control of the sample temperature (or some other critical process parameter) as a function of time would be employed to allow for varying etch conditions depending on the layer composition. This will be of particular

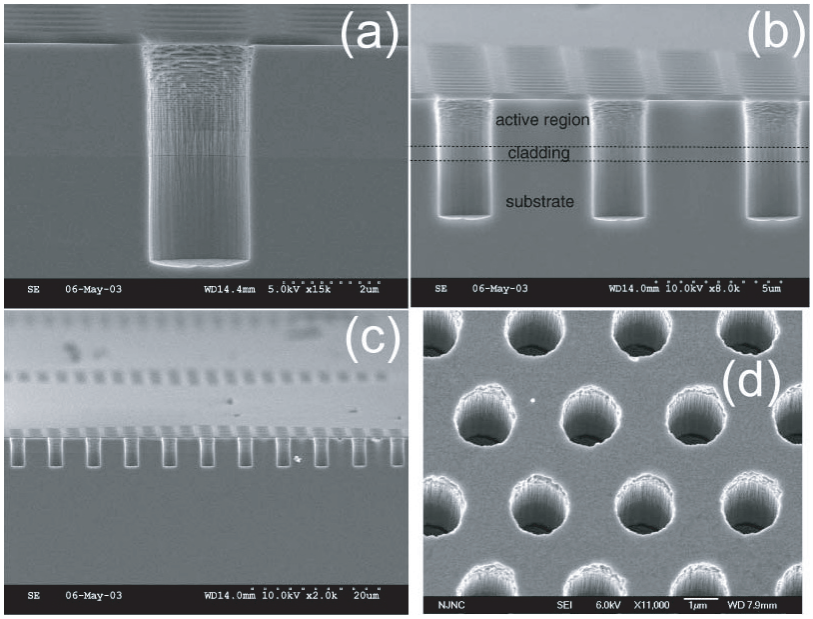

Figure C.8: SEM images of a typical QC-PCSEL device after the semiconductor etch, but before the deposition of electrical contacts. (a)-(c) Images of a cleaved device at different magnifications, showing (a) the verticality and relative smoothness of the etch, (b) the etch depth compared to the active region thickness of the QC device, and (c) the uniformity of the etch across the whole device. (d) SEM image of a device from the top surface.

use in standard vertical waveguide designs that have both top and bottom semiconductor cladding layers (often composed of AlInAs).

Appendix D

Cavity Q and Related Quantities

There are a number of physical quantities related to a cavity quality factor (Q) that appear in the literature. I have made an attempt to summarize some of these quantities in this appendix.

The definition of a cavity's quality factor is essentially $Q = \omega\tau_{ph}$, where ω is the cavity mode frequency and τ_{ph} is the photon lifetime within the cavity ($\tau_{ph} = 1/\Delta\omega$, where $\Delta\omega$ is the spectral width of the cavity mode). Q is defined in terms of the energy of the field, so that $1/\tau_{ph} = \omega/Q$ is an energy decay rate. The field's decay rate is one-half this amount, so that:

$$\kappa = \frac{\omega}{2Q}. \tag{D.1}$$

Written like this, κ has units of radians/second. To convert this to Hz, we divide by 2π. I have tried to adopt the convention of explicitly writing $\kappa/2\pi$ when quoting cavity decay rates in units of Hz, to avoid any confusion.

It is sometimes convenient to consider a cavity decay length L_{ph}, which can be defined through

$$\tau_{ph} = \frac{L_{ph}}{c/n} \tag{D.2}$$

where c/n is the speed of light within the cavity. More precisely, n is not the material refractive index but instead is the group index of the mode within the cavity, n_g. The Q of the cavity can be written in terms of L_{ph} as:

$$Q = \frac{2\pi n_g L_{ph}}{\lambda} \tag{D.3}$$

Typically, a decay length L_{ph} might not be quoted, but rather, an inverse decay length $\alpha = L_{ph}^{-1}$ is. This is in particular true for structures such as waveguides, for which a loss per unit length (sometimes in units of cm^{-1} for example, and other times in units such as dB/cm) is a common metric. Equation (D.3) above is then important for being able to compare waveguide loss to a cavity Q. Perhaps more important, material absorption losses are often quoted in terms of a loss per unit length, and equation (D.3) then tells us how to compute the equivalent absorption-limited Q.

A cavity's Q physically represents the number of cycles the optical field undergoes before its energy decay to a value that is $1/e$ time its original value. This is nothing more than saying that the cavities energy decays in time as $e^{-\omega t/Q}$, or equivalently

$$\frac{dU}{dt} = -\frac{\omega}{Q}U \tag{D.4}$$

Where U is the stored energy within the cavity, and $P_d = -\frac{dU}{dt}$ is the dissipated power. This leads to another common definition of Q,

$$Q = \omega\frac{U}{P_d} \tag{D.5}$$

If we write the cavity frequency $\omega = \frac{2\pi}{T}$, where T is period of the field, this equation can be re-written as

$$Q = 2\pi\frac{U}{U_{l,c}} \tag{D.6}$$

where $U_{l,c}$ is the energy loss per cycle (period). For traveling wave mode cavities, such as Fabry-Perots or WGM-based devices, it is common to quote a cavity finesse F , which is given by

$$F = \frac{U}{U_{l,rt}} \tag{D.7}$$

where $U_{l,rt}$ is the energy loss per round trip length (where the round trip length is $2L$ for a Fabry-Perot cavity of length L and $2\pi R$ for a WGM cavity of radius R). The finesse is then related to the Q (modulo 2π) by the ratio of $U_{l,c}$ to $U_{l,rt}$. This ratio is simply the number of optical cycles within a round trip length L_{rt}, which is $L_{rt}/(\lambda/n_g)$. Plugging into equation (D.7), we have:

$$F = \frac{Q}{2\pi}\frac{\lambda}{n_g L_{rt}} \tag{D.8}$$

Finally, our equation for the decay length L_{ph} (equation (D.3)), can be used to simply write the finesse as:

$$F = \frac{L_{ph}}{L_{rt}} \tag{D.9}$$

A cavity finesse of 1 then means that the field decays to its $1/e$ point after one complete round trip.

Appendix E

Resonator-Waveguide Coupled Mode Theory

In this appendix, I briefly review some of the key equations of the coupling of modes in time approach of Haus et al. [125] that is often used to study resonator-waveguide coupling. There are many references that treat this topic; the discussion below has been primarily influenced by refs. [50, 57, 55]. Other helpful works include refs. [214, 215, 216].

E.1 Traveling wave mode resonator

We first consider coupling between a single mode waveguide and a single mode of a cavity; an example of this would be coupling between the forward propagating mode of a waveguide and the clockwise propagating WGM of a microdisk resonator, as shown in fig. E.1. The cavity's intrinsic loss rate is γ_i, and its loss rate into the waveguide is γ_e. Note that the γ's are energy decay rates,

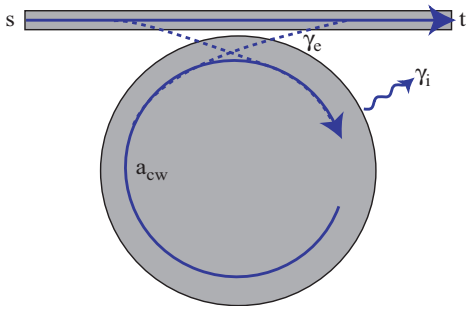

Figure E.1: Schematic for single mode coupling between a resonator and waveguide. The cavity's intrinsic energy loss rate is γ_i, and its energy loss rate into the waveguide is γ_e. The cavity, whose mode amplitude is called a_{cw}, is excited by a waveguide mode s, and the transmitted field past the cavity is t. Note that a_{cw} is normalized to energy, while s and t are normalized to power.

related to the field decay rates by a factor of 2, as discussed in appendix D. The waveguide input field is labeled s, and it couples to a cavity mode of amplitude a_{cw}. The transmitted field past the cavity is t, with s and t normalized to power, and a_{cw} normalized to energy [125].

The time evolution of the mode amplitude a_{cw} is given by:

$$\frac{da_{cw}}{dt} = i\omega_0 a_{cw} - \frac{\gamma_T}{2} a_{cw} + k_e s \tag{E.1}$$

where γ_T is the total energy decay rate of the cavity mode (equal to γ_0+γ_e above), and k_e is the waveguide-resonator coupling coefficient.[1] The above equation simply states that the mode amplitude a_{cw} oscillates in time with a frequency ω_0 (first term on the right hand side), decays with a loss rate γ_T (second term), and is driven by an input field s with coupling coefficient k_e (third term).

The transmitted signal t will have a contribution due to that portion of the input signal s that does not couple into the cavity, and a contribution from the signal coupled out of the cavity. We thus expect $t = \alpha_1 s + \alpha_2 a_{cw}$, where α_1 and α_2 are coefficients to be determined. We can determine α_1 and α_2 through a power conservation argument, where we equate the power transfer into the cavity with the change in the cavity's internal energy plus the dissipated power. That is, we write:

$$|s|^2 - |t|^2 = \frac{d|a_{cw}|^2}{dt} + \gamma_0 |a_{cw}|^2 \tag{E.2}$$

Plugging in equation (E.1) along with $t = \alpha_1 s + \alpha_2 a_{cw}$ yields three equations for the variables α_1 and α_2 (which are complex). We have

$$\begin{aligned} 1 - |\alpha_1|^2 &= 0 \\ |\alpha_2|^2 &= \gamma_e \\ -\alpha_1 \alpha_2^* &= k_e \end{aligned} \tag{E.3}$$

One simple choice of solution is α_1=-1, $\alpha_2 = k_e^*$ (with $|k_e|^2 = \gamma_e$), giving the transmitted signal as:

[1] Coupling coefficients are often denoted by the symbol κ. However, we have already reserved κ for the field decay rate, so we choose k instead.

$$t = -s + k_e^* a_{cw} \tag{E.4}$$

From equations (E.1) and (E.4), we can find the steady state (normalized) transmission through the waveguide, given by $T = |\frac{t}{s}|^2$. Before doing this, we expand our formalism a bit to let $\gamma_T = \gamma_e + \gamma_0 + \gamma_p$, where γ_p is a loss term representing parasitic coupling between the waveguide and resonator (for example, coupling-induced scattering into radiation modes). From this, we solve for T, and arrive at:

$$T = \left| \frac{\gamma_e - (\gamma_0 + \gamma_p) - 2i\Delta\omega}{\gamma_e + (\gamma_0 + \gamma_p) + 2i\Delta\omega} \right|^2 \tag{E.5}$$

where $\Delta\omega = \omega - \omega_0$, the difference between the drive frequency and the cavity resonance frequency. As a function of ω, T is a Lorentzian centered at $\omega = \omega_0$.

On resonance (Δω=0), we can rewrite this equation as

$$T = \left(\frac{1-K}{1+K}\right)^2 \tag{E.6}$$

where K is called the coupling parameter [55, 57], and is defined as

$$K = \frac{\gamma_e}{\gamma_0 + \gamma_p} \tag{E.7}$$

K is the ratio of coupling into the waveguide with coupling into intrinsic and parasitic loss channels. K=1 is called critical coupling (corresponding to complete power transfer, where waveguide-cavity coupling equals intrinsic and parasitic loss), while $K < 1$ ($K > 1$) is called the undercoupled (overcoupled) regime. These important regimes are discussed in many other works [125, 20, 55, 214].

Experimentally, we always measure $Q_T = \omega_0/\gamma_T$, although we have control over γ_e by controlling the taper-cavity separation. In practice, we can increase the taper-cavity separation to the point that γ_e is quite small, giving us an estimate of the cold-cavity quality factor Q_i (assuming that γ_p

also becomes quite small as the separation becomes large). Without changing the taper-cavity separation, we can get an estimate of Q_{i+p}, the Q due to intrinsic decay and parasitic waveguide-cavity coupling, by knowing K, or equivalently, the transmission depth on resonance (equation (E.6)). In particular,

$$\begin{aligned} Q_{i+P} = \frac{\omega_0}{\gamma_0+\gamma_p} &= \frac{\omega_0}{\gamma_0+\gamma_e+\gamma_p} \cdot \frac{\gamma_0+\gamma_e+\gamma_p}{\gamma_0+\gamma_p} \\ &= Q_T(1+K) \end{aligned} \tag{E.8}$$

Another important parameter is called the ideality I, which is the ratio of the coupling into the waveguide mode of interest with the coupling into all waveguide channels. That is,

$$I = \frac{\gamma_e}{\gamma_e+\gamma_p} \tag{E.9}$$

I=1 implies that the resonator-waveguide coupling is ideal in the sense that all coupling is into the desired waveguide channel.

Next, let us consider the case of an emitter within the cavity. A fraction β of the emitter's spontaneous emission will be coupled into the cavity mode of interest. The fraction of these photons that are then coupled into the waveguide mode of interest is given by the parameter η_0, with

$$\eta_0 = \frac{\gamma_e}{\gamma_e+\gamma_0+\gamma_p} \tag{E.10}$$

This can easily be rewritten in terms of the coupling parameter K as:

$$\eta_0 = \frac{1}{1+1/K} \tag{E.11}$$

We see that η_0 approaches unity as the system is driven into the overcoupled regime; at critical coupling (K=1), $\eta_0 = 50\%$. In the literature, much attention is paid to β, with a high-β cavity often seen as a solution to efficiently collecting photons from an emitter, such as a self-assembled quantum dot within a high-index semiconductor. Although it is somewhat obvious, we note here

that η_0 also plays an important role, with $\beta\eta_0$ giving the total fraction of emitted photons that are actually collected into the channel of interest, which could be the forward propagating fundamental taper mode in our experiments, or some well-defined free-space collection channel for experiments with a Fabry-Perot cavity.

The ratio of the total (loaded) quality factor Q_T to the intrinsic quality factor Q_i can be written in terms of η_0 and I as:

$$\begin{aligned}\frac{Q_T}{Q_i} = \frac{\gamma_0}{\gamma_0+\gamma_e+\gamma_p} &= \frac{\gamma_0+\gamma_e+\gamma_p}{\gamma_0+\gamma_e+\gamma_p} - \frac{\gamma_e+\gamma_p}{\gamma_0+\gamma_e+\gamma_p} \\ &= 1 - \frac{\gamma_e}{\gamma_e+\gamma_0+\gamma_p}\frac{\gamma_e+\gamma_p}{\gamma_e} \\ &= 1 - \frac{\eta_0}{I}\end{aligned} \tag{E.12}$$

Finally, we consider two quantities of importance to many processes that occur within optical microcavities. The internal cavity energy U can be written as the product of the dropped power into the cavity, P_d, and the photon lifetime due to intrinsic and parasitic losses, τ_{i+P}. Noting that $P_d = (1-T)P_{in}$, where P_{in} is the input power into the waveguide, and plugging in for T in terms of the coupling parameter K, we have:

$$\begin{aligned}U &= (1-T)P_{in}\tau_{i+P} \\ &= \frac{4K}{(1+K)^2}P_{in}\frac{Q_{i+P}}{\omega_0} \\ &= \frac{4K}{1+K}P_{in}\frac{Q_T}{\omega_0}\end{aligned} \tag{E.13}$$

Equations (E.12) and (E.11) can then be used to relate U to the intrinsic quality factor Q_i, ideality I, and coupling parameter K. This yields:

$$U = \frac{4K}{(1+K)^2}(I+K(I-1))\frac{Q_i}{\omega_0}P_{in} \tag{E.14}$$

This quantity is maximized when $K = I/(2-I)$, for which $U = I(Q_i/\omega_0)P_{in}$.

The circulating intensity within the cavity, $\Im$, is given as $\Im = (U/V_{\text{eff}})v_g$, where v_g is the group index of the cavity mode. For critical coupling ($K = 1$) with unity ideality ($I = 1$), we can simply

write this as:

$$\begin{aligned}\Im &= v_g \frac{U}{V_{\text{eff}}} \\ &= \frac{c}{n_g}\frac{Q_i}{\omega_0 V_{\text{eff}}} P_{in} \\ &= P_{in}\frac{\lambda_0}{2\pi n_g}\frac{Q_i}{V_{\text{eff}}}\end{aligned} \tag{E.15}$$

E.2 Standing wave mode resonator

We next briefly consider the case where the resonator supports a standing wave mode rather than a traveling wave mode. This is true, for example, in the photonic crystal microcavities studied in the first part of this thesis. The main difference is that the standing wave mode decays equally into the forward *and* backward propagating modes of the waveguide. If we continue to consider γ_e to be the loss rate into the forward propagating waveguide mode, the total loss rate γ_T is given as $\gamma_T = 2\gamma_e + \gamma_0 + \gamma_p$. The formula for the normalized transmission is then determined through an analogous set of equations as used above, with:

$$T = \left| \frac{\gamma_e - (\gamma_e + \gamma_0 + \gamma_p) - 2i\Delta\omega}{\gamma_e + (\gamma_e + \gamma_0 + \gamma_p) + 2i\Delta\omega} \right|^2 \tag{E.16}$$

On resonance ($\Delta\omega$=0), we can rewrite this equation as:

$$T = \left(\frac{1-K}{1+K}\right)^2 \tag{E.17}$$

where the coupling parameter K is now written as

$$K = \frac{\gamma_e}{\gamma_e + \gamma_0 + \gamma_p} \tag{E.18}$$

We see that the form of $T(K)$ is exactly the same as what is was for coupling to a traveling wave mode, but the range of values that K can attain is restricted to $K \leq 1$.

In coupling to a standing wave mode, there is now a reflected signal coming out of the input

port, with the normalized reflection R given as $R = |\frac{r}{s}|^2$. In this equation, $r = k_e^* a_{sw}$, where a_{sw} is the standing wave mode amplitude. We then arrive at:

$$R = \left| \frac{2\gamma_e}{\gamma_e + (\gamma_e + \gamma_0 + \gamma_p) + 2i\Delta\omega} \right|^2 \tag{E.19}$$

so that on resonance, this is rewritten in terms of K as:

$$R = \frac{4K^2}{(1+K)^2} \tag{E.20}$$

Finally, we consider the parameter η_0. Assuming that photons are only collected from one of the waveguide modes, it is defined as:

$$\eta_0 = \frac{\gamma_e}{2\gamma_e + \gamma_0 + \gamma_p} \tag{E.21}$$

and can again be rewritten in terms of the coupling parameter K as:

$$\eta_0 = \frac{1}{1+1/K} \tag{E.22}$$

provided that K is defined as in equation (E.18). We see that $\eta_0 \leq 50\%$, which makes sense because the cavity mode equally decays into the forwards and backwards channels of the waveguide, so that at most 50% of the cavity photons can be collected out of any one channel. For the experiments we have conducted thus far (chapters 6 and 7), collection from both channels can be easily achieved, so that this is not a significant limitation. However, this might not always be the case, particularly if the cavity-waveguide unit is to be a node within a more complex system.

Appendix F

Laser Rate Equations

A rate equation approach [152, 217, 218] is often a simple way to study aspects of the steady state and dynamical behavior of lasers. Although a full quantum mechanical approach can be more rigorous, rate equation techniques are typically relatively simple and easier to solve, while still including fluctuations (i.e., spontaneous emission into the laser mode), albeit at a relatively basic level. In contrast, purely semi-classical theories, beginning at the level of the Maxwell-Bloch equations, for example, neglect fluctuations altogether [219]. In what follows, we present an overview of a simple rate equation model used in the fits of our 2 μm diameter microdisk-quantum-dot lasers studied in chapter 7. There are a number of good treatments of rate equation modeling in the literature; I have personally benefitted from studying the text of Coldren and Corzine [152].

For semiconductor lasers, the rate equations are often a pair of equations that describe the time evolution of the carrier number (N) and photon number in the cavity mode of interest (N_p) within the structure. Here, we are considering a semiconductor material where light emission occurs as a result of electron-hole recombination, and where the active material maintains charge neutrality, so that the electron number N_e is equal to the hole number N_h, and we keep track of a single carrier number N. The rate of change of N will be given by the difference between carrier generation processes and carrier recombination processes. Carrier generation (occurring at a rate L) can occur through current injection or optical pumping, for example. Recombination processes can include stimulated and spontaneous emission (R_{st} and R_{sp}) and non-radiative recombination (R_{nr}) (carrier leakage can also be a factor, although we do not consider it here). Calling the volume of the active region V, we can write this explicitly as:

$$\frac{dN}{dt} = L - (R_{nr} + R_{sp} + R_{st})V \tag{F.1}$$

The rate of change of N_p will be given by difference in photon generation and photon removal processes. Photon generation will be due to stimulated and spontaneous emission, while photon removal will be due to cavity loss. We can write this equation as:

$$\frac{dN_p}{dt} = (R_{st} + \beta R_{sp})V - \frac{N_p}{\tau_{ph}} \tag{F.2}$$

where $\gamma_{ph} = 1/\tau_{ph}$ is the photon number loss rate from the cavity (=ω/Q). As we have mentioned in other parts of this thesis, β is called the spontaneous emission coupling factor, and is the fraction of spontaneous emission emitted into the cavity mode of interest. In this equation, we have not explicitly made use of the modal confinement factor Γ, which basically takes into account the fact that the volume of the cavity mode of interest will often be different than the volume of the active region. This is because our equations are in terms of carrier number and photon number; if we had instead written them in terms of densities, use of Γ would be necessary, because the photon number N_p is not taken over the active region volume V, but rather a mode volume.

From this point, an essentially phenomenological approach is often used to describe the different recombination processes; the specifics often depend on the gain medium under consideration. For our purposes in chapter 7, the gain medium is a single layer of quantum dots. Let us first consider stimulated recombination R_{st}. By a stimulated process, we mean that photon generation requires the presence of seed photons. It is therefore taken to be proportional to the photon number N_p; for example, $R_{st} = v_g g_l N_p$ as in Coldren and Corzine [152], where v_g is the group velocity of the cavity mode and g_l is the gain per unit length. Equivalently, it can be written in terms of a gain per unit time g as $R_{st} = gN_p$. Next, the spontaneous recombination term R_{sp} is often taken to be a bi-particle process (electron-hole recombination), so that $R_{sp} = BN^2$, where B is called the bimolecular recombination rate. Non-radiative recombination is usually a combination of processes with varying power law dependencies on N. One process is surface recombination, which is often taken as $R_{sr} = AN$, where A is some material-dependent coefficient. Another process is Auger recombination, the transfer of kinetic energy from an electron-hole pair to another electron (or

hole). It is often taken as $R_A = CN^3$, where C is called the Auger recombination coefficient.

The rate equations we use to model the microdisk lasers of chapter 7 are:

$$\frac{dN}{dt} = L - [\frac{N^{1.22}}{\tau_s} + \frac{N^2}{\tau'_{sp}}] - gN_p \tag{F.3}$$

$$\frac{dN_p}{dt} = (g - \gamma_{ph})N_p + \frac{\beta N^2}{\tau'_{sp}} \tag{F.4}$$

Here, we have assumed an N^2 dependence for radiative recombination, no Auger recombination, and have taken the surface recombination term to have a $N^{1.22}$ dependence (as discussed in chapter 7, this is done to match the measured subthreshold slope of the light-in-light-out curve). In these equations, the proportionality coefficients in front of the N-dependent terms have been written as lifetimes, with τ_s being the surface recombination lifetime and τ'_{sp} being the Purcell-factor-modified (appendix H) spontaneous emission lifetime of the quantum dots (where the unmodified lifetime is taken to be 1 ns).

In our microdisk cavities, carrier generation is accomplished through optical pumping, where the measured quantity is the pump power incident on the sample surface, P_{inc}. L is related to P_{inc} through:

$$L = \frac{P_{inc}\eta_{abs}\eta_{int}}{E_{ph,pump}} \frac{A_m}{A_{pump}} \tag{F.5}$$

where η_{abs} is the fraction of incident pump power that is absorbed, η_{int} is the internal efficiency of carrier generation, $E_{ph,pump}$ is the energy per pump photon, A_m is the modal area, and A_{pump} is the pump beam area. Basically, $P_{inc}\eta_{abs}A_m/A_{pump}$ gives the absorbed pump power by the disk, dividing by $E_{ph,pump}$ converts this to an absorbed photon number rate, and multiplying by η_{int} converts this to a carrier generation rate.

The surface recombination lifetime τ_s is taken as:

$$\tau_s = \frac{1}{2(2\pi R\rho_{A,QD})v_s} \tag{F.6}$$

Here, $\rho_{A,QD}$ is the areal quantum dot density, a quantity estimated by the material growers (300

μm^{-2} for the QD material we use), so that $2\pi R\rho_{A,QD}$ gives a linear QD density along the perimeter of the device (the additional factor of 2 in the equation takes into account the degeneracy of the QD ground state). v_s is a surface recombination velocity, which we take as a fit parameter.

The gain per unit time g is taken to have the form:

$$g = g'(N - N_{tr}) \tag{F.7}$$

where g' is the differential gain and $N_{tr} = \rho_{A,QD}A_m$ is the transparency carrier number (the total number of available states is $2\rho_{A,QD}A_m$ due to degeneracy, and the transparency level is half of this). g' is taken to be the maximum modal gain if all QD ground states interacting with the cavity mode are inverted divided by the total number of QD states.

We thus solve the rate equations (equation (F.3)) in steady state to give us the steady state photon number $N_{p,ss}$ as a function of pump power. To match our experimental data, the collected laser power (L_{out}) is related to $N_{p,ss}$ through:

$$L_{out} = \eta_{coll}E_{ph}\gamma_{ph}N_{p,ss} \tag{F.8}$$

where E_{ph} is the emitted photon energy ($E_{ph} = \hbar\omega$) and η_{coll} is the collection efficiency. Finally, we have:

$$\eta_{coll} = \xi\frac{E_{ph,pump}}{E_{ph}}\eta_{int} \tag{F.9}$$

where ξ is the laser's differential efficiency (which we directly measure, as discussed in chapter 7), and $E_{ph,pump}/E_{ph}$ is the ratio of the energies of the pump and emission photons. The steady state solutions to the rate equations, using the relationships outlined above, produce the solid fits to the experimental data in fig. 7.8.

Appendix G

The Jaynes-Cummings Model

The interaction of an atom with an electromagnetic field is approached in a number of different ways, depending on how the atom and field are treated (classically or quantum mechanically). Semiclassical models treat the field classically and the atom quantum mechanically. The Jaynes-Cummings model [220, 221, 222] treats both quantum mechanically, but makes several simplifying assumptions. In particular, the atom is treated as a two-level system, and driving and dissipation terms are not included. In this appendix, I first briefly review the Jaynes-Cummings model. I then consider extensions of this model to include driving and damping terms, following the quantum master equation approach as outlined by Carmichael in his books [149, 180].

G.1 The Jaynes-Cummings Hamiltonian and eigenvalue spectrum

The Jaynes-Cummings Hamiltonian H_{JC} can be written as:

$$H_{\mathrm{JC}} = H_{\mathrm{atom}} + H_{\mathrm{field}} + H_{\mathrm{int}}, \tag{G.1}$$

where H_{atom}, H_{field}, and H_{int} are terms due to the free atom, the free field, and the atom-field interaction, respectively. The first two terms can be written as:

$$H_{\mathrm{atom}} = \frac{1}{2}\hbar\omega_a\hat{\sigma}_z \quad H_{\mathrm{field}} = \hbar\omega_f\left(\hat{a}^\dagger\hat{a} + \frac{1}{2}\right) \tag{G.2}$$

where $\hat{\sigma}_z$ is the Pauli spin operator (inversion), ω_a and ω_f are the atomic transition and electromagnetic field frequencies, and $\hat{a}$ ($\hat{a}^\dagger$) is the electromagnetic field annihilation (creation) operator. The

$\frac{1}{2}\hbar\omega_f$ term is often left out of the free-field Hamiltonian, as it is just adds a constant energy shift to the eigenstates.

The dipole interaction term is $H_{\text{int}} = -\hat{\mathbf{d}}\cdot\hat{\mathbf{E}}$, where $\hat{\mathbf{d}}$ is the dipole operator, and can be written as $\hat{\mathbf{d}} = \mathbf{d}_{eg}|e><g| + \mathbf{d}^*_{eg}|g><e|$. Here, $|g>$ and $|e>$ are the ground and excited states of the atom, and we have assumed that they are states of definite parity, so that the dipole operator only contains off-diagonal terms. The terms $|e><g|$ and $|g><e|$ are just the Pauli matrices σ_+ and σ_-, so that:

$$\hat{\mathbf{d}} = \mathbf{d}_{eg}\hat{\sigma}_+ + \mathbf{d}^*_{eg}\hat{\sigma}_- \tag{G.3}$$

Quantizing the electromagnetic field [223], we write the electric field operator as:

$$\hat{\mathbf{E}}(\mathbf{r}) = iE_{max}\left(\mathbf{f}(\mathbf{r})\hat{a} - \mathbf{f}^*(\mathbf{r})\hat{a}^\dagger\right) \tag{G.4}$$

where $\mathbf{f}(\mathbf{r})$ describes the spatial variation of the electric field (it is essentially a normalized version of the electric field), and E_{max} is the amplitude of the field (see appendix H). From this equation, along with the expression for $\hat{\mathbf{d}}$, we write the interaction term H_{int} as

$$H_{\text{int}} = i\hbar g(\hat{a}^\dagger\hat{\sigma}_- - \hat{a}\hat{\sigma}_+) \tag{G.5}$$

where g is the atom-field coupling rate, which we consider in further detail in appendix H. In this equation for H_{int}, we have neglected the $\hat{a}\sigma_-$ and $\hat{a}^\dagger\sigma_+$ terms, which are processes that do not conserve energy (the former process corresponds to annihilation of a photon while having the atom transition from the excited to the ground state, for example). This is essentially the rotating wave approximation. Thus, our final form for the Jaynes-Cummings Hamiltonian, including all three terms, is:

$$H_{\text{JC}} = \frac{1}{2}\hbar\omega_a\hat{\sigma}_z + \hbar\omega_f\left(\hat{a}^\dagger\hat{a} + \frac{1}{2}\right) + i\hbar g(\hat{a}^\dagger\hat{\sigma}_- - \hat{a}\hat{\sigma}_+) \tag{G.6}$$

The energy eigenvalues of this system can be determined by considering product states of the

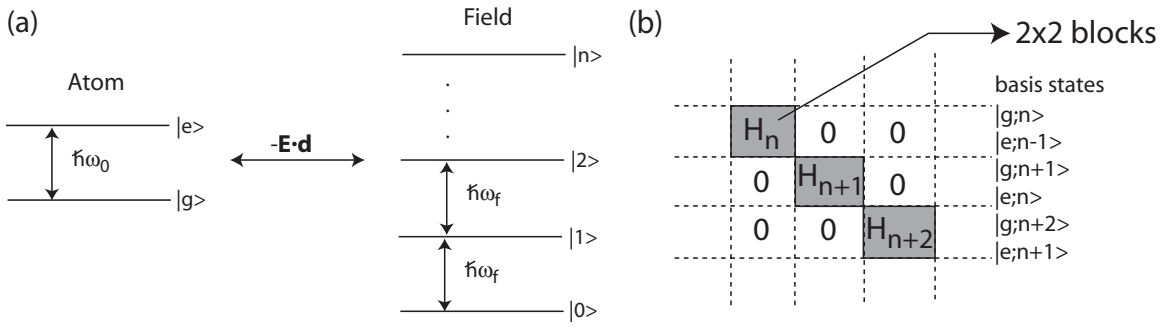

Figure G.1: (a) Schematic for atom-field coupling and (b) block diagonal form for the Hamiltonian in the Jaynes-Cummings model.

form $|g;k>$ ($|g;k>=|g>\otimes|k>$), where the atom is in either the excited or ground state, and the field has k photons. We have:

$$H_{\rm JC}|g;n>=-\frac{1}{2}\hbar\omega_a|g;n>+\hbar\omega_f\left(n+\frac{1}{2}\right)|g;n>-i\hbar g\sqrt{n}|e;n-1> \tag{G.7}$$

$$H_{\rm JC}|e;n-1>=\frac{1}{2}\hbar\omega_a|e;n-1>+\hbar\omega_f\left(n-\frac{1}{2}\right)|e;n-1>+i\hbar g\sqrt{n}|g;n>. \tag{G.8}$$

In matrix form, the Hamiltonian is block diagonal, with 2x2 blocks. The form for the nth block (fig. G.1(b)) is:

$$H_n=\hbar\begin{pmatrix}(n+\frac{1}{2})\omega_f-\frac{\omega_a}{2} & -ig\sqrt{n}\\ ig\sqrt{n} & (n-\frac{1}{2})\omega_f+\frac{\omega_a}{2}\end{pmatrix}. \tag{G.9}$$

The eigenvalues for this matrix are

$$E_{n,\pm}=\hbar\left(n\omega_f\pm\frac{\Omega}{2}\right) \tag{G.10}$$

$$\Omega=\sqrt{(\omega_f-\omega_a)^2+4ng^2} \tag{G.11}$$

The corresponding eigenstates, which we write as $|n,\pm>$, are mixtures of $|g;n>$ and $|e;n-1>$:

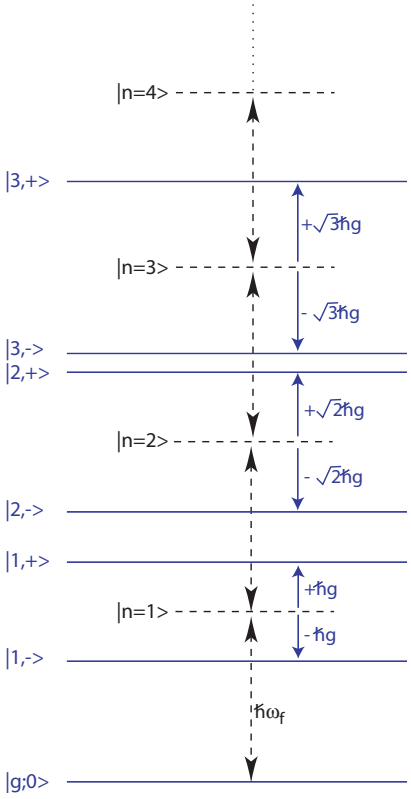

Figure G.2: Energy level spectrum for the Jaynes-Cummings model ($\omega_f = \omega_a$). The unperturbed field states are shown as black dashed horizontal lines and are labeled as $|n = 1>$, for example. The eigenstates of the Jaynes-Cummings Hamiltonian are labeled as $|n, \pm>$, and are shown as solid horizontal lines.

$$|n,->= -\sin\theta_n|g;n> +\cos\theta_n|e;n-1> \tag{G.12}$$

$$|n,+>= \cos\theta_n|g;n> +\sin\theta_n|e;n-1> \tag{G.13}$$

$$\tan(2\theta_n) = \frac{2g\sqrt{n}}{\omega_f - \omega_a} \tag{G.14}$$

From this, we see that for vary large detunings, or alternately, very small coupling strengths g, the eigenstates are essentially product states.

On-resonance ($\omega_f = \omega_a$), the eigenvalues and eigenstates are:

$$E_{n,\pm} = \hbar\left(n\omega_f \pm g\sqrt{n}\right) \tag{G.15}$$

$$|n,->= -\frac{1}{\sqrt{2}}\left(|g;n> -|e;n-1>\right) \tag{G.16}$$

$$|n,+>= \frac{1}{\sqrt{2}}\left(|g;n> +|e;n-1>\right). \tag{G.17}$$

The eigenvalue spectrum for the coupled atom-field system (on-resonance) is shown schematically

in fig. G.2. We see that the field's harmonic oscillator spectrum, consisting of energy levels separated by $\hbar\omega_f$, has been modified, with each energy level splitting into a pair of levels, separated by a spacing of $\Delta E = 2g\sqrt{n}$. The splitting of the first excited state (n=1) is $2g$, and is called the vacuum Rabi splitting.

G.2 The damped, driven Jaynes-Cummings model

The Jaynes-Cummings Hamiltonian of the previous section examines the interaction of a single mode electromagnetic field (such as the mode of an electromagnetic cavity) with a two-level atom, and basically models an isolated system. An experiment will typically differ from this in two primary ways. There will often be some probe field that is used to study the system; the probe might be a weak classical field that is swept in frequency, for example. In addition, the atom-cavity system will be unavoidably coupled to the environment, which will cause dissipation. This may come in the form of cavity loss or spontaneous emission of the atom, for example. In this section, we review how the Jaynes-Cummings model is expanded to account for these effects.

G.2.1 Driving field

From the previous section, we recall that the Jaynes-Cummings Hamiltonian is written as:

$$H_{\mathrm{JC}} = \frac{1}{2}\hbar\omega_a\hat{\sigma}_z + \hbar\omega_c\left(\hat{a}^\dagger\hat{a} + \frac{1}{2}\right) + i\hbar g(\hat{a}^\dagger\hat{\sigma}_- - \hat{a}\hat{\sigma}_+) \tag{G.18}$$

where here we have relabeled the field to oscillate at frequency ω_c, to explicitly indicate that we are considering it to be the mode of an electromagnetic cavity. The driving field modifies H_{JC} by adding a term H_{drive}, given as:

$$H_{\mathrm{drive}} = i\hbar\left[E\begin{bmatrix}\hat{\sigma}_+\\ \hat{a}^\dagger\end{bmatrix}e^{-i\omega_l t} - E^*\begin{bmatrix}\hat{\sigma}_-\\ \hat{a}\end{bmatrix}e^{i\omega_l t}\right] \tag{G.19}$$

where E and ω_l are the amplitude and frequency of the driving field. The top row in the equation (involving $\hat{\sigma}_+$ and $\hat{\sigma}_-$) applies to the case of the field driving the atom, and the bottom row (involving $\hat{a}^\dagger$ and $\hat{a}$) is when the field drives the cavity mode. The introduction of this time-dependent term

into the Hamiltonian can be handled by transforming to a frame that rotates at the same frequency as the driving field (ω_l). That is, we will apply a unitary transformation $\hat{U} = \exp(-i\omega_l t(\hat{\sigma}_z/2 + \hat{a}^\dagger\hat{a}))$. In general, we know that if some unitary operator $\hat{U}$ acts on the state vector, the transformed Hamiltonian, H_r, is written in terms of the original Hamiltonian H_S as [224]:

$$H_\mathrm{r} = i\hbar\dot{\hat{U}}\hat{U}^\dagger + \hat{U}H_\mathrm{S}\hat{U}^\dagger. \tag{G.20}$$

We apply this to the Hamiltonian $H_\mathrm{S} = H_\mathrm{JC} + H_\mathrm{drive}$, and make use of the operator expansion theorem [225]:

$$\exp(x\hat{A})\hat{B}\exp(-x\hat{A}) = \hat{B} + x[\hat{A},\hat{B}] + \frac{x^2}{2!}[\hat{A},[\hat{A},\hat{B}]] + \ldots \tag{G.21}$$

This yields the following form for the driven Jaynes-Cummings Hamiltonian (written in a frame rotating at ω_l):

$$H_\mathrm{r} = \hbar\Delta\omega_{al}\hat{\sigma}_+\hat{\sigma}_- + \hbar\Delta\omega_{cl}\hat{a}^\dagger\hat{a} + i\hbar g(\hat{a}^\dagger\hat{\sigma}_- - \hat{a}\hat{\sigma}_+) + i\hbar\left[E\begin{bmatrix}\hat{\sigma}_+\\ \hat{a}^\dagger\end{bmatrix} - E^*\begin{bmatrix}\hat{\sigma}_-\\ \hat{a}\end{bmatrix}\right] \tag{G.22}$$

where $\Delta\omega_{cl} = \omega_c - \omega_l$ and $\Delta\omega_{al} = \omega_a - \omega_l$. In deriving this equation, we have noted that $\hat{\sigma}_+\hat{\sigma}_- = (I + \hat{\sigma}_z)/2$. As described in ref. [226], the addition of the driving term to the Jaynes-Cummings Hamiltonian can modify the eigenvalue spectrum considerably. In particular, when the cavity is driven by the external field, the energy levels undergo a driving-field-dependent Stark shift, with the standard Rabi splittings of $\pm g\sqrt{n}$ being replaced by the quasienergies $\pm g\sqrt{n}[1-(2E/g)^2]^{3/4}$ (when the atom, cavity, and driving field all at the same frequency). This can have a direct impact on experiments, where the atom-cavity system is often probed by a driving field that is swept in frequency [9, 182]. If the probe beam has a small amplitude (where the ratio of E to g is the important metric), its effects on the atom-cavity system would be expected to be small, and measurements of features such as vacuum Rabi splitting should yield the $2g$ splitting in accordance with the Jaynes-Cummings model.[1] However, if the probe beam has a large amplitude, the energy level structure of

[1] The $2g$ splitting of the first excited state is maintained down to an arbitrarily weak driving field E; this is one reason for the terminology 'vacuum Rabi splitting'.

the Jaynes-Cummings model will be significantly altered. This can, for example, affect the ability to access and observe higher excited states of the Jaynes-Cummings system.

G.2.2 Dissipation terms and the quantum master equation approach

Dissipation in the Jaynes-Cummings system can be addressed by considering the interaction of this system with a reservoir. The treatment we follow below is entirely based on Carmichael's books [149, 180]. Our intent here is to briefly outline some of the important steps in this approach.

The Hamiltonian for the system plus reservoir is given as $H_S + H_R + H_{SR}$, where H_S and H_R are system and reservoir Hamiltonians, and H_{SR} is the Hamiltonian for the interaction of the two [180]. The interest in the reservoir is purely in terms of its effects on the system, so that a density matrix approach is well suited to study this problem. In particular, rather than considering the full density matrix of the system plus reservoir χ, a reduced density matrix $\rho = Tr_R[\chi]$ is considered, where the trace is taken over all of the reservoir states.

As χ is a density matrix, we know that:

$$\frac{d\chi}{dt} = \frac{1}{i\hbar}[H, \chi]. \tag{G.23}$$

A convenient form for the equation of motion of χ can be determined by first transforming to the interaction picture to separate out the motion due to $H_S + H_R$ from that due to H_{SR}, and then formally integrating equation (G.23) to arrive at:

$$\frac{d\tilde{\chi}}{dt} = \frac{1}{i\hbar}[\tilde{H}_{SR}, \tilde{\chi}(0)] - \frac{1}{\hbar^2}\int_0^t dt'[\tilde{H}_{SR}(t), [\tilde{H}_{SR}(t'), \tilde{\chi}(t')]]. \tag{G.24}$$

Here, the $\sim$ is to note that all of the quantities are in the interaction picture. Our interest is in the reduced density matrix ρ, which is found by tracing over the reservoir states, so that:

$$\frac{d\tilde{\rho}}{dt} = -\frac{1}{\hbar^2}\int_0^t dt' Tr_R\Big[[\tilde{H}_{SR}(t), [\tilde{H}_{SR}(t'), \tilde{\chi}(t')]]\Big]. \tag{G.25}$$

The first term from equation (G.24) has been dropped (it can essentially be thought of as a constant offset in the Hamiltonian). From this point, two important simplifying assumptions are made. The

first is called the Born Approximation, where we assume that the total density matrix (χ) can be written as the product of density matrices for the system (ρ) and reservoir R, and furthermore, that the effect of the system on the reservoir is negligible, so that R does not vary in time ($R(t) = R(0)$). This yields:

$$\frac{d\tilde{\rho}}{dt} = -\frac{1}{\hbar^2}\int_0^t dt' Tr_{\rm R}\Big[[\tilde{H}_{\rm SR}(t),[\tilde{H}_{\rm SR}(t'),\tilde{\rho}(t')R(0)]]\Big]. \tag{G.26}$$

The second major simplifying assumption is the Markov approximation, where we assume a memoryless system behavior due to the interaction with the reservoir. Carmichael's books consider this point in much greater detail [149, 180]. Assuming this point to be valid, its effect on equation (G.26) is to change the $\tilde{\rho}(t')$ within the integrand to $\tilde{\rho}(t)$.

From this point, specific models for the system, reservoir, and system-reservoir interaction Hamiltonians are employed. Many times, the reservoir is modeled as a collection of harmonic oscillators. The system-reservoir interaction Hamiltonian will often be written as $H_{\rm SR} = \hbar\sum_j s_j\Gamma_j$ where s and Γ are system and reservoir operators, respectively. System operators might be the field annihilation and creation operators $\hat{a}$ and $\hat{a}^\dagger$, or atomic raising and lowering operators $\hat{\sigma}_+$ and $\hat{\sigma}_-$, for example. Reservoir operators might be of the form $\Gamma = \sum_j \kappa_j \hat{r}_j$, for example, where the κ_j is the coupling coefficient linking the jth reservoir oscillator (characterized by annihilation and creation operators $\hat{r}_j$ and $\hat{r}_j^\dagger$) to the field.

For the systems of interest to us, there are three primary dissipative channels: (i) atomic spontaneous emission, at a rate $\gamma_\parallel$, into modes other than the cavity mode of interest, (ii) photon leakage out of the cavity at a rate 2κ (so that the cavity's field decay rate is κ, as in appendix D), and (iii) non-radiative damping through phase-destroying processes, at a rate γ_p. These loss terms are given by [149, 180]:

$$L_1\tilde{\rho} = \kappa(2\hat{a}\tilde{\rho}\hat{a}^\dagger - \hat{a}^\dagger\hat{a}\tilde{\rho} - \tilde{\rho}\hat{a}^\dagger\hat{a}) \tag{G.27}$$

$$L_2\tilde{\rho} = \frac{\gamma_\parallel}{2}(2\hat{\sigma}_-\tilde{\rho}\hat{\sigma}_+ - \hat{\sigma}_+\hat{\sigma}_-\tilde{\rho} - \tilde{\rho}\hat{\sigma}_+\hat{\sigma}_-) \tag{G.28}$$

$$L_3\tilde{\rho} = \frac{\gamma_p}{2}(\hat{\sigma}_z\tilde{\rho}\hat{\sigma}_z - \tilde{\rho}). \tag{G.29}$$

The equation for the reduced density matrix in the interaction picture is then:

$$\frac{d\tilde{\rho}}{dt} = (L_1 + L_2 + L_3)\tilde{\rho}. \tag{G.30}$$

Finally, we need to transform back to the Schrodinger picture from the interaction picture. We do this by noting that

$$\tilde{\rho}(t) = e^{\frac{iH_S t}{\hbar}} \rho(t) e^{-\frac{iH_S t}{\hbar}} \tag{G.31}$$

so that differentiating this equation yields:

$$\dot{\tilde{\rho}}(t) = e^{\frac{iH_S t}{\hbar}} \dot{\rho}(t) e^{-\frac{iH_S t}{\hbar}} + \frac{i}{\hbar}[H_S, \tilde{\rho}] \tag{G.32}$$

$$e^{\frac{-iH_S t}{\hbar}} \dot{\tilde{\rho}}(t) e^{\frac{iH_S t}{\hbar}} = \dot{\rho}(t) + \frac{i}{\hbar}[H_S, \rho] \tag{G.33}$$

$$\dot{\rho} = \frac{1}{i\hbar}[H_S, \rho] + e^{\frac{-iH_S t}{\hbar}} \dot{\tilde{\rho}}(t) e^{\frac{iH_S t}{\hbar}} \tag{G.34}$$

Putting it all together, we get the following master equation for the density matrix, often used as a starting point in cavity QED studies:

$$\frac{d\rho}{dt} = \frac{1}{i\hbar}[H_S, \rho] + \kappa(2\hat{a}\rho\hat{a}^\dagger - \hat{a}^\dagger\hat{a}\rho - \rho\hat{a}^\dagger\hat{a}) \tag{G.35}$$

$$+ \frac{\gamma_\parallel}{2}(2\hat{\sigma}_-\rho\hat{\sigma}_+ - \hat{\sigma}_+\hat{\sigma}_-\rho - \rho\hat{\sigma}_+\hat{\sigma}_-) \tag{G.36}$$

$$+ \frac{\gamma_p}{2}(\hat{\sigma}_z\rho\hat{\sigma}_z - \rho) \tag{G.37}$$

with

$$H_S = \hbar\Delta\omega_{al}\hat{\sigma}_+\hat{\sigma}_- + \hbar\Delta\omega_{cl}\hat{a}^\dagger\hat{a} + i\hbar g(\hat{a}^\dagger\hat{\sigma}_- - \hat{a}\hat{\sigma}_+) + i\hbar\left[E\begin{bmatrix}\hat{\sigma}_+ \\ \hat{a}^\dagger\end{bmatrix} - E^*\begin{bmatrix}\hat{\sigma}_- \\ \hat{a}\end{bmatrix}\right]. \tag{G.38}$$

From this master equation, the time evolution of operator expectation values can be easily found by noting that $< \hat{A} >= Tr(\hat{\rho}\hat{A})$ and $< \dot{\hat{A}} >= Tr(\hat{\rho}\dot{\hat{A}})$ for a system operator $\hat{A}$. For example, if the driving field excites the cavity, these time-evolution equations are (here, we take $\hbar = 1$):

$$\frac{d}{dt} < \hat{a} >= -\Big(i\Delta\omega_{cl} + \kappa\Big) < \hat{a} > + g < \hat{\sigma}_{-} > + E \tag{G.39}$$

$$\frac{d}{dt} < \hat{\sigma}_{-} >= -\Big(i\Delta\omega_{al} + \gamma_{\perp}\Big) < \hat{\sigma}_{-} > + g < \hat{\sigma}_{z}\hat{a} > \tag{G.40}$$

$$\frac{d}{dt} < \hat{\sigma}_{z} >= -2g(< \hat{\sigma}_{-}\hat{a}^{\dagger} > + < \hat{\sigma}_{+}\hat{a} >) - \gamma_{\parallel}(1 + < \hat{\sigma}_{z} >) \tag{G.41}$$

To derive these equations, the identities $[\hat{\sigma}_{+}, \hat{\sigma}_{-}] = \hat{\sigma}_{z}$, $\hat{\sigma}_{+}\hat{\sigma}_{-} + \hat{\sigma}_{-}\hat{\sigma}_{+} = I$, and $\hat{\sigma}_{\pm}^{2}$=0 are useful, as is utilizing the cyclic property of the trace operator ($Tr(\hat{A}\hat{B}\hat{C}) = Tr(\hat{C}\hat{A}\hat{B}) = Tr(\hat{B}\hat{C}\hat{A})$). In addition, we have taken $\gamma_{\perp} = \gamma_{\parallel}/2 + \gamma_{p}$.

In the semi-classical limit, expectation values of operator products are replaced by products of operator expectation values (i.e., $< \hat{\sigma}_{z}\hat{a} >=< \hat{\sigma}_{z} >< \hat{a} >$). These Maxwell-Bloch equations can then be solved in steady state, for example, to yield the optical bistability state equation (OBSE) [181, 182]. For reference, the solution is:

$$X = \frac{Y}{1 + \frac{2C}{X^{2} + (\frac{\Delta\omega_{al}}{\gamma_{\perp}})^{2} + 1} + i\Big(\frac{\Delta\omega_{cl}}{\kappa} - \frac{2C\Big(\frac{\Delta\omega_{al}}{\gamma_{\perp}}\Big)}{X^{2} + (\frac{\Delta\omega_{al}}{\gamma_{\perp}})^{2} + 1}\Big)} \tag{G.42}$$

where

$$\begin{aligned} n_{s} &= \frac{\gamma_{\perp}\gamma_{\parallel}}{4g^{2}}, \\ C &= \frac{g^{2}}{2\kappa\gamma_{\perp}}, \\ Y &= \frac{E}{\kappa} n_{s}^{-1/2}, \\ X &=< \hat{a} > n_{s}^{-1/2}. \end{aligned} \tag{G.43}$$

n_{s} and C are called the saturation photon number and critical atom number (also known as the single atom cooperativity), which represent the number of photons (on average) needed to saturate the atomic transition and the number of atoms needed to dramatically affect the response of the cavity, respectively [9].

Appendix H

The Purcell Factor F_p and Atom-Photon Coupling Rate g

H.1 The Purcell factor

The degree to which a microcavity can influence the spontaneous rate of an emitter within it is known as the Purcell effect [227]. When the emitter (a radiating dipole) is on resonance with a cavity mode, this rate can be enhanced; when off-resonance, it can be inhibited [228]. Purcell enhancement (or inhibition) of spontaneous emission if one of the hallmarks of cavity QED within the *weak coupling* regime, where it is still appropriate to treat the emitter and the field as separate entities and their interaction as a perturbation. In *strong coupling*, the usual interpretation of spontaneous emission as an irreversible process no longer holds. The Jaynes-Cummings model reviewed in appendix G is the starting point for the treatment of emitter-field interactions in the strong coupling regime.

Placing a radiating dipole within a cavity causes the spontaneous emission rate to change due to the cavity's modification of the spectral density of modes (related to its Q) and the amplitude of the vacuum field interacting with the dipole (related to V_{eff}). We therefore expect the Purcell enhancement to scale with Q and V_{eff}. A simple derivation of this enhancement has been given by Gérard and Gayral [109]; we repeat this derivation here. We begin with the statement of Fermi's Golden Rule [224]:

$$\frac{1}{\tau_{\text{sp}}} = \frac{2\pi}{\hbar^2}|W_{ge}|^2\rho(E_{ge}) \tag{H.1}$$

W_{ge} is the dipole matrix element between the initial (ground) and final (excited) states of the two-

level system, with

$$W_{ge} = < \hat{\mathbf{d}} \cdot \hat{\mathbf{E}} >_{ge} \tag{H.2}$$

where **d** is the electric dipole operator, **E** is the electric field operator, and the subscript *ge* indicates that the matrix element connects the ground and excited states of the emitter. $\rho(E_{ge})$ is the density of photon modes at the emitter's transition energy E_{ge}. We recall that Fermi's Golden Rule is only applicable under the assumption that the dipole can effectively be thought of as coupling to a continuum of modes. When the dipole is embedded in a uniform dielectric material, this is clearly the case. When it is embedded within a cavity, we must satisfy the condition that the dipole's emission line be spectrally narrow compared to the cavity resonance.

Let us begin by calculating the spontaneous emission rate when the emitter is in a uniform dielectric of index *n*. The density of modes ρ is obtained by the usual procedure of counting the number of modes within some box of volume *V* [224]. This yields:

$$\rho_0 = \frac{\omega^2 n^3 V}{3\pi^2 c^3} \tag{H.3}$$

where the factor of 1/3 represents the random orientation of the modes within a uniform dielectric with respect to the dipole (this factor is derived in Yariv's Quantum Electronics book [223], for example). The spontaneous emission rate is then given by:

$$\frac{1}{\tau_{sp,0}} = \frac{2\pi}{\hbar^2} | < \hat{\mathbf{d}} \cdot \hat{\mathbf{E}} >_{ge} |^2 \frac{\omega^2 n^3 V}{3\pi^2 c^3} \tag{H.4}$$

with the electric field operator written as [223]

$$\hat{\mathbf{E}}(\mathbf{r}) = iE_{max}\left(\mathbf{f}(\mathbf{r})\hat{a} - \mathbf{f}^*(\mathbf{r})\hat{a}^\dagger\right) \tag{H.5}$$

In this equation, $\hat{a}$ and $\hat{a}^\dagger$ are the field annihilation and creation operators, respectively, and $\mathbf{f}(\mathbf{r})$ is describes the spatial variation of the electric field (it is essentially a normalized version of the

electric field). E_{max} is the amplitude of the field, a per photon electric field strength written as:

$$E_{max} = \sqrt{\frac{\hbar\omega}{2\varepsilon_0 n^2 V}} \tag{H.6}$$

If we plug this into equation (H.4), we arrive at:

$$\frac{1}{\tau_{sp,0}} = \frac{ne^2|\hat{\mathbf{r}}_{ge}|^2\omega^3}{3\pi\hbar\varepsilon_0 c^3} \tag{H.7}$$

where I have taken $\hat{\mathbf{d}} = e\mathbf{r}$. Equation (H.7) is the standard expression for the spontaneous emission rate into a uniform dielectric material of index n.

When the emitter is placed in a cavity with a mode volume V_{eff}, E_{max} is given by the same expression as in equation (H.6), but with V (the quantization volume for the uniform dielectric material) replaced by V_{eff}. We next write $|W_{ge}|^2 = e^2|\hat{\mathbf{r}}_{ge}|^2 E_{max}^2 \eta^2$, where $\eta = \mathbf{d}\cdot\mathbf{E}/|\mathbf{d}|E_{max}$ describes not only the orientation of the dipole with respect to the cavity field, but also the spatial dependence of the dipole within the cavity field (that is, even if the dipole is aligned with the field, if it is positioned at some place other than an antinode of the field, $\eta < 1$). If the cavity mode has a linewidth $\Delta\omega_c$, corresponding to a quality factor $Q = \omega_c/\Delta\omega_c$, we can write its density of states as:

$$\rho_c = \frac{2Q}{\pi\omega_c}\frac{\Delta\omega_c^2}{4(\omega-\omega_c)^2+\Delta\omega_c^2} \tag{H.8}$$

which is a Lorentzian function that has been normalized so that $\int_\omega \rho_c(\omega)d\omega = 1$. If we plug this, along with our expression for $|W_{ge}|^2$ into equation (H.1), we arrive at:

$$\frac{1}{\tau_{sp,c}} = \frac{2Qe^2|\hat{\mathbf{r}}_{ge}|^2\eta^2}{\hbar\varepsilon_0 n^2 V_{\text{eff}}}\frac{\Delta\omega_c^2}{4(\omega-\omega_c)^2+\Delta\omega_c^2} \tag{H.9}$$

The ratio of equations H.9 and H.7 gives us the Purcell enhancement:

$$\frac{\tau_{sp,0}}{\tau_{sp,c}} = \frac{3}{4\pi^2}\left(\frac{Q}{V_{\text{eff}}}\right)\left(\frac{\lambda}{n}\right)^3\frac{\Delta\omega_c^2}{4(\omega-\omega_c)^2+\Delta\omega_c^2}\eta^2 \tag{H.10}$$

When the emitter is spatially aligned with an antinode of the field, is spectrally aligned with the field ($\omega = \omega_c$), and oriented along the field, we arrive at the Purcell factor F_p quoted in chapter 4:

$$F_p = \frac{\tau_{sp,0}}{\tau_{sp,c}} = \frac{3}{4\pi^2}\left(\frac{Q}{V_{\text{eff}}}\right)\left(\frac{\lambda_c}{n}\right)^3 \tag{H.11}$$

We again note that the above is valid when the dipole emission linewidth is narrow in comparison to the cavity mode linewidth. If this is not the case, the Q used in F_p will not be the cavity Q but instead will be the emitter's $Q = \lambda_e/\gamma_e$, where γ_e is the emitter linewidth.

H.2 Atom-photon coupling rate

The coupling strength between a single two-level system and an optical field is given by the dipole matrix element divide by Planck's constant. That is:

$$g = \frac{|<\hat{\mathbf{d}}\cdot\hat{\mathbf{E}}>|}{\hbar} \tag{H.12}$$

For the purposes of this thesis, the above formula is used to calculate quantities like the optimal coupling strength between an atom, or quantum dot, and a single photon within a resonant cavity. For these calculations, it is assumed that the dipole and the field are aligned, so that $g = d_{ge}E_{max}/\hbar$, where the per photon field strength E_{max} of equation (H.6) is used, along with some value for the strength of the electric dipole d_{ge} as found in literature.

In many cases, d_{ge} will not be the piece of information readily available; rather, the spontaneous emission rate between the two levels τ_{sp} will be. Using equation (H.7), we can easily relate the two quantities, and then arrive at an expression for g. Doing so yields

$$g = \frac{1}{2\tau_{\text{sp}}}\sqrt{\frac{3c\lambda_0^2\tau_{\text{sp}}}{2\pi n^3 V_{\text{eff}}}}, \tag{H.13}$$

As defined above, g has units of radians/second; dividing by 2π express it units of Hz, which are often the units for which g is quoted. To be explicit, I have adopted the convention of writing $g/2\pi$ when quoting values in units of Hz, to try to eliminate any confusion.

Within the literature, the decay rates $\gamma_{\|}$ and $\gamma_{\perp}$ are sometimes used. $\gamma_{\|}$ is a radiative decay rate, equal to $1/\tau_{sp}$. $\gamma_{\perp}$ is a transverse decay rate, and is most generally written as $\gamma_{\perp} = \frac{\gamma_{\|}}{2} + \gamma_p$, where γ_p is due to non-radiative decay (for example, phase-destroying collisional processes). For strong coupling, it is the total emitter decay rate, $\gamma_{\perp}$, that must be exceeded by the coherent coupling rate g. Within single atom systems, the decay is essentially purely radiative, so that $\gamma_{\perp} = \frac{\gamma_{\|}}{2}$ is taken. For these systems, g is then often written in terms of $\gamma_{\perp}$ rather than τ_{sp}. Doing so yields

$$g = \gamma_{\perp}\sqrt{\frac{3c\lambda_0^2}{4\pi n^3 V_{\text{eff}}\gamma_{\perp}}}, \tag{H.14}$$

Within the literature, the decay times T_1 and T_2 are often quoted [223]; by our definitions above, $T_2 = 1/\gamma_{\perp}$ and $T_1 = 1/\gamma_{\|}$.

In semiconductor-based structures such as quantum dots, an oscillator strength is often quoted [110, 70]. This oscillator strength f is a dimensionless quantity given by

$$f = \frac{2m\omega|<\hat{\mathbf{r}}_{ge}>|^2}{\hbar}, \tag{H.15}$$

It is found through a calculation of the optical susceptibility $\chi(\omega)$ of an atom ($P(\omega) = \chi(\omega)E(\omega)$, where $P(\omega)$ is the field-induced polarization), and subsequent comparison to the expression generated by the classical damped, driven harmonic oscillator model of the atom. Reference [229] presents such a derivation. The QD-coupling rate g can then be written in terms of the oscillator strength as:

$$g = \sqrt{\frac{e^2 f}{4\varepsilon_0 n^2 V_{\text{eff}}}}, \tag{H.16}$$